

## Technique for visualization and quantification of three dimensional intracellular ion measurements in vascular endothelial cells

Charles W. Patrick Jr. and Larry V. McIntire

Citation: [Review of Scientific Instruments](#) **66**, 2476 (1995); doi: 10.1063/1.1145645

View online: <http://dx.doi.org/10.1063/1.1145645>

View Table of Contents: <http://scitation.aip.org/content/aip/journal/rsi/66/3?ver=pdfcov>

Published by the [AIP Publishing](#)

---

### Articles you may be interested in

[Quantification of stromal vascular cell mechanics with a linear cell monolayer rheometer](#)

J. Rheol. **59**, 33 (2015); 10.1122/1.4902437

[Migration and vascular lumen formation of endothelial cells in cancer cell spheroids of various sizes](#)

Biomechanics **8**, 052109 (2014); 10.1063/1.4895568

[A microdevice for the creation of patent, three-dimensional endothelial cell-based microcirculatory networks](#)

Biomechanics **5**, 034115 (2011); 10.1063/1.3609264

[Ultrasound standing wave fields induce endothelial cell sprouting within three-dimensional engineered tissue.](#)

J. Acoust. Soc. Am. **127**, 1940 (2010); 10.1121/1.3384887

[Measurement and visualization of three-dimensional directivity pattern](#)

J. Acoust. Soc. Am. **118**, 1861 (2005); 10.1121/1.4778916

---

The advertisement has a dark blue background with abstract circular patterns. On the left, there is a circular inset image of a man with glasses and a beard, wearing a lab coat, looking at a piece of equipment. To the right of the image, the text reads: 'On the way to a graphene spin field effect transistor' in large white font. Below this, in smaller white font, it says 'by Prof. Barbaros and the Özyilmaz Group at National University of Singapore'. In the top right corner, the Oxford Instruments logo is displayed, consisting of the word 'OXFORD' above 'INSTRUMENTS' inside a white rectangular box, with the tagline 'The Business of Science®' below it. At the bottom right, there is an orange rectangular button with the text 'Download a FREE application note' in white.

# Technique for visualization and quantification of three dimensional intracellular ion measurements in vascular endothelial cells

Charles W. Patrick, Jr. and Larry V. McIntire<sup>a)</sup>

Cox Laboratory for Biomedical Engineering, Rice University, Houston, Texas 77251

(Received 7 March 1994; accepted for publication 30 October 1994)

A first generation digital imaging video microscopy system has been developed that is able to provide both quantitative and visual three dimensional information from individual vascular endothelial cells. More specifically, with the combination of optical sectioning, video microscopy, digital image processing and analysis, deconvolution, fluorescence ratio imaging, and scientific visualization we are able to measure the dynamic changes in spatial distributions of intracellular ions. The technique presented involves the following steps: acquiring three dimensional biological data by optical sectioning of a specimen, preprocessing the digitized volume data, experimentally determining the digital imaging system's point spread function (PSF), deconvolving the volume data with the PSF to remove the inherent out-of-focus information, and finally postprocessing and volume rendering in order to display the volume data in a quantitative and comprehensible manner. This technique permits high resolution visualization and quantification of three dimensional spatial distributions of ions as well as traditional temporal changes in ion concentration. It has the potential to aid immensely in research since the three dimensional spatial information is often a prerequisite for understanding the molecular mechanisms involved in many complex cellular processes.

© 1995 American Institute of Physics.

## I. INTRODUCTION

Vascular endothelial cells alter their structure and metabolism in response to the hemodynamic forces generated by blood flow.<sup>1-19</sup> The exact signal transduction pathways by which these cells recognize mechanical loading are not yet known. It is known, however, that some intracellular ions can undergo dynamic changes when cells are stimulated by both mechanical and biochemical perturbations. These ions may serve as second messengers. Since many diseases are the direct result of dysfunction in signal transduction pathways, investigation into the various mechanisms involved is warranted. The ultimate goal would be to generate pharmaceuticals that block or mimic the action of second messengers to correct the dysfunctions. In fact, Spencer *et al.*<sup>20</sup> have recently reported the control of signal transduction in a T cell line by using synthetic ligands to activate and terminate specific intracellular signal transmissions to modulate expression of a specific target gene. This ligand regulated activation and termination may be used to allow precise control of pharmaceutical action on vascular endothelial cells once the signal transduction pathways in the cells have been elucidated.

Conventional fluorescence microscopy can quantitate ion distributions in only a single two dimensional section of a cell. At best one is able to determine average regional values for the ion concentrations within a cell. Cells are loaded with an ion specific dye whose fluorescence is proportional to the ion concentration. Temporal changes in ion concentration are then obtained by acquiring images of fluorescence intensity of a single two dimensional section as a

function of time. Although this method gives important and valuable data, it is difficult to attain all the information concerning intracellular biological mechanisms by merely collecting data in two dimensions. If anything, the two dimensional information collected thus far proves that molecular signaling mechanisms are even more complex than originally perceived. One needs to go beyond knowing merely what the average concentration of a particular ion is in the cytoplasm relative to the cell's nucleus and plasma membrane. One needs to be able to determine where in the cell's three dimensional architecture the ion changes begin to occur (near the cytoplasmic membrane where channels and receptors are or in the vicinity of particular internal organelles) and how the ion changes propagate through the cell (do they spiral through the cell, form spherical waves, or are there just local changes). Software and hardware technology as well as quantification techniques are now readily available and moderately priced to allow one to obtain three dimensional biological data. Three dimensional spatial distributions of ion concentrations are needed if we are to begin approaching complete understanding of biological mechanisms. The ability to collect three dimensional data has become a prerequisite rather than a scientific luxury.

There are primarily two widely used optical methods by which to acquire three dimensional information from biological specimens—confocal microscopy and optical sectioning microscopy. Confocal microscopy has been used to acquire high resolution, three dimensional images of a variety of cellular components, including cytoskeletal elements and DNA. However, confocal microscopy is not the method of choice for acquiring three dimensional ion distributions for several reasons. The scanning speed of a laser through a volume has proven to be too slow to capture the dynamic changes of intracellular ions in many cases compared to the speed of optical sectioning. More specifically, a laser confo-

<sup>a)</sup>Address all correspondence to Dr. Larry V. McIntire, Cox Laboratory for Biomedical Engineering, Institute of Biosciences and Bioengineering, Rice University, Houston, TX 77251-1892.

cal system images a single voxel whereas optical sectioning images a full 2D slice of a volume (247 808 voxels for a 512×484 slice). In addition, the laser emissions are too intense to be used for many dyes without causing photobleaching and photodamage, the laser wavelengths available to date do not lend themselves to the use of many of the most common fluorescent dyes (like the  $\text{Ca}^{2+}$  specific dye Fura-2), the quantum efficiency of confocal microscopy detectors are low (0.1–0.35) compared to the SITs and CCDs (0.6–0.8) used in optical sectioning,<sup>21</sup> and confocal microscopy is fairly expensive compared to a more versatile microscopy system equipped with optical sectioning.

Images obtained by optical sectioning, however, are inherently contaminated with out-of-focus information, leaving one with visually blurred images which can lead to incorrect quantification of ion concentrations. Confocal microscopy implicitly removes most of the out-of-focus information by using a pin hole aperture, but optical sectioning microscopy must rely on explicit methods. Computational image restoration algorithms (deconvolution) based on the optical equations of image formation are employed to “deblur” or remove the out-of-focus contamination. Optical sectioning coupled with image restoration techniques has proven to give higher resolution and a better signal to noise ratio (S/N) than confocal microscopy.<sup>21</sup> There have been several deconvolution algorithms employed in the past such as inverse filtering,<sup>22–24</sup> Wiener filtering,<sup>22–26</sup> nearest neighbor deblurring,<sup>22–24,26–28</sup> no neighbor deblurring,<sup>29</sup> constrained iterative deconvolution with non-negativity constraints (Jansson–vanCittert deconvolution method),<sup>22–26,30–32</sup> solving Toeplitz systems based on projection onto convex sets,<sup>33</sup> and noniterative regularized methods based on linear precision gauge theory.<sup>33,34</sup> Our first algorithm used the Jansson–vanCittert deconvolution method. However, the amount of out-of-focus information in Fura-2 loaded cells was too great to remove without incorporating excessive noise in the solution or causing divergence in the solution. Others have also reached the same conclusion.<sup>21,35</sup> Therefore, we elected to adopt an iterative regularization method with non-negativity constraints that is based on convex analysis.<sup>21,35–38</sup>

The entire technique presented is composed of three steps: data acquisition, deconvolution, and volume visualization. Each step of the technique will be discussed in detail as well as results of various tests on the implementation of the technique. The accuracy and applicability of this technique was first tested on one and two dimensional computer phantoms. The computer phantoms were intentionally blurred with a model point spread function and were subsequently deblurred with a deconvolution algorithm. In addition, fluorescent beads were optically sectioned and the resulting images were deconvolved to remove out-of-focus information. Fluorescent beads were chosen as a three dimensional test specimen because they are well characterized and have a known geometry. Finally, we present the results of this technique as applied to real biological data, Fura-2 loaded vascular endothelial cells, to demonstrate the practical potential of the technique.

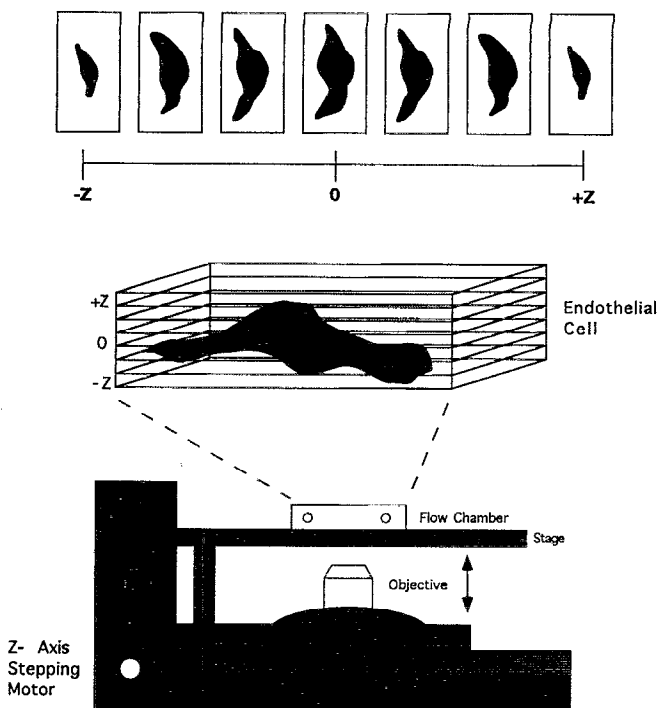


FIG. 1. Optical sectioning of a biological specimen. The z-axis stepper motor moves the objective upward, translating the focal plane through the specimen. At each focal plane a 2D image is digitized. One obtains a series of 2D slices from which a 3D image can be formed by stacking the 2D slices.

## II. THEORY OF IMAGE FORMATION AND IMAGE RESTORATION

### A. Blurring phenomena

Three dimensional information can be obtained by serially optical sectioning a specimen preloaded with a fluorescent probe used to label a particular cellular component or biochemical event. Optical sectioning consists of moving the focal plane through a specimen, usually by means of a z-axis stepper motor or a computer-controlled stage, and recording two dimensional images at each focal position along the focal axis. This is depicted in Fig. 1. Ideally, the images collected at each focal plane are in-focus versions of the specimen containing information solely from that particular plane. However, due to the limited aperture size of microscope objectives and the wave nature of light, a three dimensional distortion of the images occurs. This is manifested in the images as an overall three dimensional blurring and as a background glow that degrades the images, the latter of which is caused by the unwanted superposition of neighboring focal planes. That is to say, each of the images contains not only information from the in-focus plane, but also out-of-focus information from the remainder of the specimen. It has previously been reported that for any given image only 1%–2% of the information recorded may be derived from the in-focus plane.<sup>22</sup> The removal of the out-of-focus information that contaminates each image requires accurate knowledge of the three dimensional image forming properties of the microscope/imaging system one is using to collect data. Once the imaging properties of the system have been

characterized, a deblurring algorithm can be employed to remove the out-of-focus information. However, one must first understand how a “blurry” image is formed if one is to solve the inverse problem of removing the blurring effect; this is the subject of the next section.

## B. Three dimensional image formation

The behavior of an imaging system is best described in terms of how an idealized point source of light is distorted as it passes through an imaging system and takes on a characteristic shape called the point spread function (PSF).<sup>22,39</sup> By definition, the PSF contains all the necessary information needed to describe the optical behavior of the imaging system. The nonideality or blurring of a point source is caused by the diffraction limits of light and can be explained by the theory of wave optics. Light emitted from a point (fluorescence emission from a fluorophore, for example) is not focused to an infinitely small point in the image plane. Rather, upon passing through any of the microscope lenses, the light waves undergo constructive and destructive interference to produce a three dimensional diffraction pattern. If a particular image plane of the three dimensional diffraction pattern is examined, a characteristic two dimensional diffraction pattern is observed, called an Airy disk.<sup>40,41</sup> Airy disks consist of a small bright spot surrounded by progressively dimmer light and dark concentric rings. The light and dark rings are due to constructive and destructive interference, respectively. If one assumes for a moment that a specimen lays entirely in a single two dimensional plane, then its image would consist of the superposition of all the Airy disks produced by each individual point in the specimen plane.<sup>42</sup> However, once the third dimension is considered, one must realize that light emitted from a point source is not bounded only to one particular plane. Rather, light extends outward in all directions, crossing many focal planes before the wave energy is quenched. Hence, there will be contributions from point sources above and below the specimen plane. This is what causes the majority of the haze and blurring seen in fluorescent images.

There are many optical components of an imaging system that contribute to the particular shape of the PSF. The principle optical components affecting the PSF are the excitation lamp collector lens, the excitation filters, the neutral density filters, the dichroic mirror, the objective, the glass coverslip on the flow chamber, the frequency of light emitted from the probe, and the emission filter. In addition, image intensifiers present in acquisition devices contribute to the PSF. Of these, the objective lens is the primary contributor to the PSF's shape. This is especially true for epifluorescence where the objective also serves as the condenser. Changes in any of the components will change the shape of the point spread function. This includes such changes as a new excitation lamp bulb, realignment of the excitation lamp, and changing the correction collar on the objective. Therefore, the PSF should be measured at the identical conditions as those used for imaging a specimen. There have been numerous attempts to derive an analytical or theoretical equation based on optical parameters such as numerical aperture and light wavelength for calculating the PSF,<sup>43–45</sup> but the best

equations to date do not agree well with experimentally determined PSFs. In fact, it has been shown that the theoretical PSF can be as much as a factor of ten different from the experimental PSF.<sup>22</sup> Thus, one is left with the task of experimentally determining the system's PSF, which is discussed in Sec. III below.

Once the point spread function is known, however, and one assumes the imaging system's signal is linear and shift invariant (for a discussion on linear, shift invariant systems and their validity refer to Young<sup>46</sup>), the observed image can be predicted by convolving the true image with the point spread function

$$o(x,y,z) = \iiint i(u,v,w) \text{psf}(x-u, y-v, z-w) \times du dv dw \quad (1)$$

or

$$o = i \otimes \text{psf}, \quad (2)$$

where  $o$  is the observed three dimensional image collected through the microscope/imaging system,  $i$  is the true or unblurred three dimensional image,  $\text{psf}$  is the characteristic point spread function, and  $\otimes$  denotes convolution. Equations (1) and (2) can be written in a more concise form by writing the equations in terms of their Fourier transforms

$$O = (I)(\text{OTF}), \quad (3)$$

where capital letters refer to Fourier transforms. The Fourier transform of the PSF is referred to as the optical transfer function (OTF). Note that the convolution process in Eqs. (1) and (2) has been simplified to multiplication in Fourier space; the advantage of this will be discussed later. The above equations state that an observed image is a result of a true image convolved with the point spread function. That is to say, each point source in the true image gets distorted in the same manner as the PSF. If one wants to obtain the true (unblurred) image from measured observed data using a measured PSF it seems a simple matter of inverting the process, that is, deconvolving the observed image with the point spread function. In Fourier space,

$$I = (O)(\text{OTF}^{-1}). \quad (4)$$

As will be discussed in Sec. IV, this simple method of reversing the blurring process by matrix inversion will not in general result in the true image volume due to amplification of noise. Thus, a more complicated restoration method must be implemented. In conclusion, the technique described below acquires the observed data, experimentally determines the PSF, and then deconvolves the observed data with the PSF using a specific algorithm to recover the true image data.

## III. EXPERIMENTAL SYSTEM AND PROCEDURES

### A. Fluorescent ratio and optical sectioning microscopy system

The equipment used in the technique presented consists of several hardware and software components which couple video fluorescence microscopy, optical sectioning, image

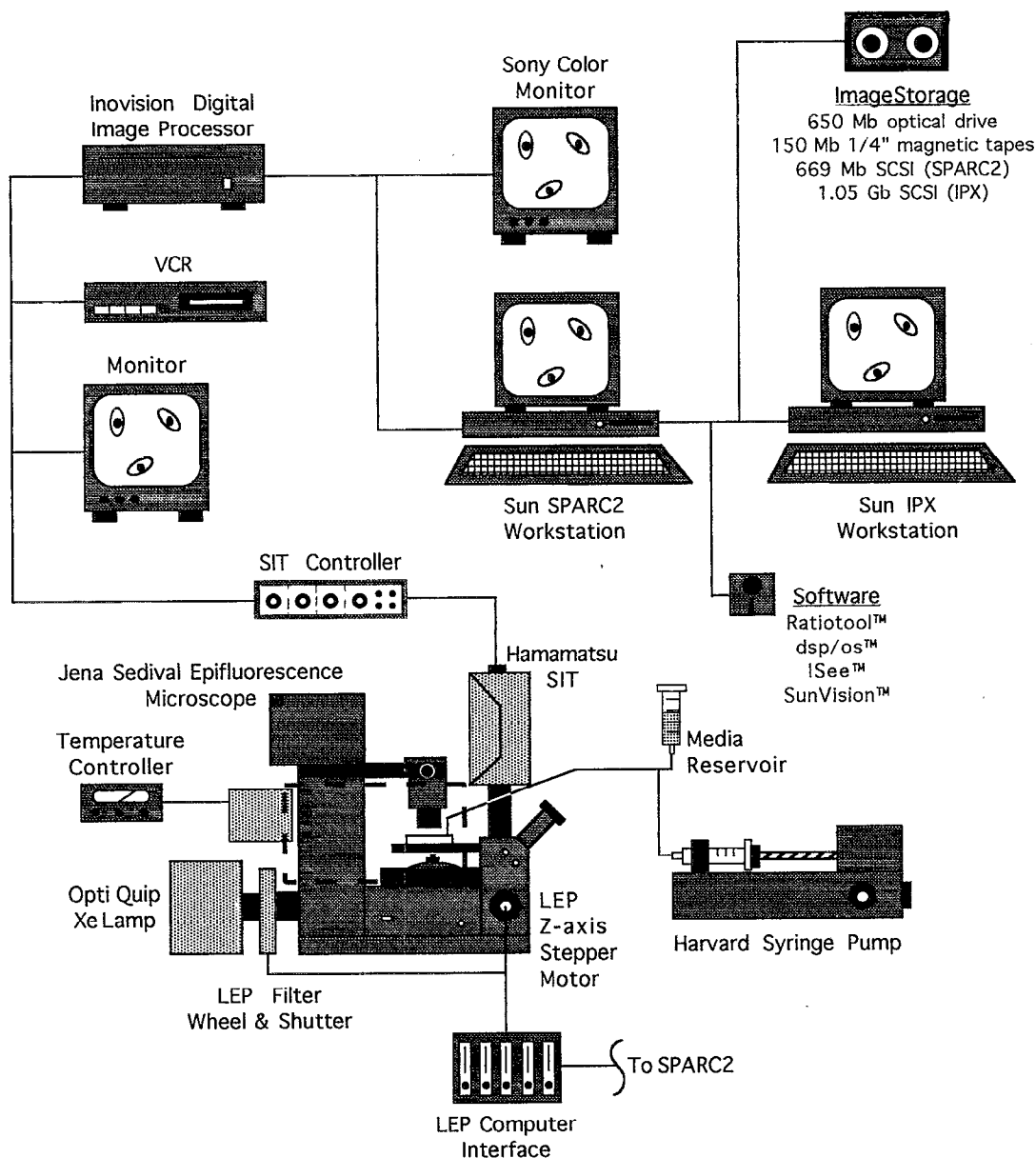


FIG. 2. Schematic of the video microscopy and digital imaging system.

processing, and scientific visualization, as shown in Fig. 2. At the heart of the microscopy system is an inverted microscope (Jena Sedival) equipped for both epifluorescence and phase contrast. The excitation illumination source is supplied by an ozone-free 150 W Xe arc lamp (Opti-Quip); a Xe arc lamp was selected because it provides a broader and more even distribution of wavelengths than does an Hg arc lamp. A shutter and filter wheel module (LEP) is mounted between the lamp housing and microscope and is computer controlled via an RS232 interface (LEP, MAC 2000 Modular Automation Controller). The high speed electromechanical shutter takes  $<5$  ms to open/close and is necessary to control the duration of excitation light exposure so as to prevent photobleaching of the fluorophores as well as to prevent constant exposure of the excitation filters to intense heat and light. The filter wheel alternates a maximum of six filter units into the excitation light path and is driven by a high speed stepper

motor, requiring  $<100$  ms to change filter positions from one adjacent position to the next. The filter units are composed of 25 mm bandpass excitation filters and any required neutral density filters with a maximum stacking thickness of 10 mm. The ability to accommodate multiple excitation filters and to change filter positions speedily allows the utilization of fluorescence ratio imaging. That is, a specimen preloaded with a fluorophore is excited at two different wavelengths and the resulting emission intensities are ratioed, thereby normalizing for nonuniform intracellular fluorophore concentration, photobleaching, probe leakage, and differences in optical path length due to changing cell thickness. For a more detailed discussion on the method of fluorescence ratio microscopy refer to Bright,<sup>47</sup> Bright *et al.*,<sup>48</sup> and Bolsover *et al.*<sup>49</sup> Emission filters and a dichroic mirror are housed in a slide bar which inserts into the microscope body. For calcium measurements using Fura-2, a 510BP40 emission filter

(Omega Optical) and a 410 dichroic mirror (MicroTech Instruments) are used. In addition, the two short bandpass excitation filters used for the ratio measurements are 340DF10 and 380DF13 (Omega Optical).

Experiments are performed using a Jena 50X, 0.95 NA Planachromat fluorite objective with a  $\infty/0.17$  working distance (MicroTech Instruments). In addition, the objective has a graduated correction collar and has a light-gathering power value of 3.8. A custom manufactured air incubator with a PID temperature controller (Omega, CN9000A) is mounted around the stage to maintain the experiment at a physiological temperature of 37 °C. The controller routinely keeps the temperature within 0.1 °C of the 37 °C setpoint. Optical sectioning is accomplished by moving the objective with a high speed microstepping motor (LEP) coupled to the microscope's fine focus control knob. The z-axis stepper motor is able to accommodate a minimum step size of 0.01  $\mu\text{m}$  and is computer controlled via the same RS232 computer interface used with the shutter and filter wheel. Emitted fluorescence is directed through the objective to a low light level SIT camera (Hamamatsu C2400-08,  $\gamma=1.0$ ). The SIT camera has low geometric distortion ( $<0.3\%$ ), low lag (7–11 frames), and potentiometers to control the gain, offset, and camera tube sensitivity. Output from the camera is routed to a digital image processing module.

The digital imaging system used is the IC-300 Modular RS-170 ROI Imaging System (Inovision). The digital imaging processing module contains Datacube's MaxVideo™ set of image processing boards. The set includes a video digitizer and display device (Digimax) which allows one to filter the analog signal with an analog low pass filter (cutoff frequencies between 2 and 10 MHz) and to adjust the analog gain (boosts between  $-4$  and 10 dB) and offset independent of the camera controller's gain and offset. In addition, a framebuffer and region-of-interest storage device (ROI-Store) is included which stores 8-bit or 16-bit images at horizontal and vertical resolutions specified by the user. A video graphics device (MaxGraph) and two general purpose signal processor devices (MaxSP and MaxMux) are also included which perform single point temporal and spatial filtering, image merging, image subtraction and addition, look-up table transformations, and minimum/maximum processing. These devices provide real time image acquisition (30 frames/s), display, and analysis capabilities. The image processing hardware is housed in an external VME cabinet and is connected to a computer workstation via a bus adapter, thus enabling direct (memory mapped) control of the image processing hardware by the workstation's CPU. Images from the image processing module can be displayed on a color monitor (Sony GVM) via RGB output or displayed directly on the computer monitor.

All the RS232 computer interfaces are connected to a SPARCstation2 Desktop Workstation (Sun Microsystems). A SPARC2 was chosen as the host computer rather than a PC in order to allow the capability of real time interfacing with experiments, image processing, and auxiliary equipment. In addition, the SPARC2 is compatible with a wide range of digital imaging and volume rendering software and allows time-sharing, multitask operating. Postprocessing, analysis,

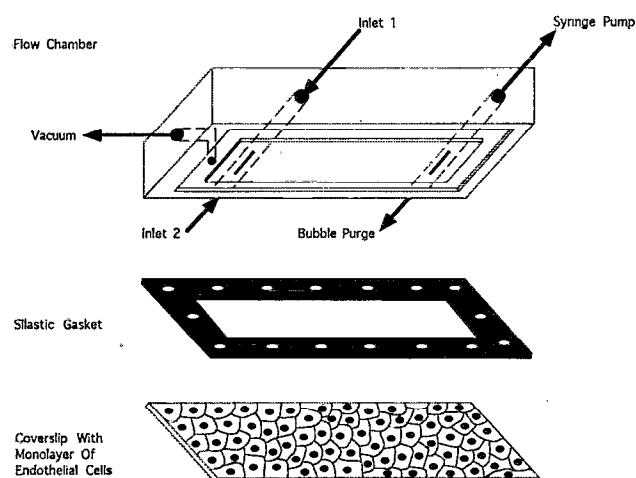


FIG. 3. Schematic of the parallel plate flow chamber.

and the deconvolution are performed on a SPARCstation IPX Desktop Workstation (Sun Microsystems) networked with the SPARC2 so that the SPARC2 could remain the primary acquisition server to maximize efficiency and real time processing, such as frame averaging and background subtraction, during acquisition. Images acquired can be stored in a number of ways: on VCR tape, on a 650 Mb optical drive (Pinnacle, PMO 650), on a 1/4 in. magnetic tape using a 150 Mb tape drive (Sun Microsystems), a 1.05 Gb external SCSI disk (Sun Microsystems) mounted on the IPX, or on a 669 Mb external SCSI disk (Sun Microsystems) mounted to the SPARC2. A number of software packages are installed including SunVision™ (Sun Microsystems) for volume rendering and scientific visualization, Ratiotool™ (Inovision) for real time acquisition and analysis of fluorescence images, dsp/os™ (Inovision) for image processing, and ISee™ (Inovision) for graphical image processing programming.

## B. Parallel plate flow chamber

To measure vascular endothelial cell metabolism in the presence of physiological hemodynamic forces a parallel plate flow chamber was utilized. The flow chamber, shown in Fig. 3, consists of a machined polycarbonate block, a Silastic gasket (0.05 cm, Dow Corning) whose thickness determines in part the channel depth, and a glass coverslip (#1, Corning) to which is attached a monolayer of endothelial cells. The individual components are held together by a vacuum, thereby ensuring a uniform channel depth. The polycarbonate block has two entry ports, a bubble port, and an exit port. Media is drawn through the chamber over the monolayer of cells using a syringe pump (Harvard Apparatus, model 915).

The use of the parallel plate flow chamber allows one to have a controlled and well defined flow environment based on the chamber geometry (fixed) and the flow rate through the chamber (variable). Assuming parallel plate geometry and Newtonian fluid behavior, the wall shear stress on the cell monolayer in the flow chamber is calculated as

$$\tau_w = \frac{6Q\mu}{bh^2}, \quad (5)$$

where  $Q$  is the volumetric flow rate ( $\text{cm}^3/\text{s}$ ),  $\mu$  is the viscosity of the flowing fluid ( $\approx 0.01 \text{ dyn s/cm}^2$ ),  $h$  is the channel height ( $0.022 \text{ cm}$ ),  $b$  is the channel width ( $1.4 \text{ cm}$ ), and  $\tau_w$  is the wall shear stress ( $\text{dyn/cm}^2$ ). Shear stress values of  $67.9$  to  $0.01$  can be obtained with the current syringe pump and gasket thickness. Experiments are typically run at a venous shear stress of  $1.4 \text{ dyn/cm}^2$  or an arterial shear stress of  $14 \text{ dyn/cm}^2$ . Data in this preliminary study were acquired under a venous shear stress. The effective volume of the flow chamber is  $123.2 \mu\text{l}$ . The Reynolds number of the flow through the chamber is given by

$$\text{Re} = \tau_w \left( \frac{h^2 \rho}{6\mu^2} \right), \quad (6)$$

where  $\rho$  is the density of the flowing media ( $\approx 1.0 \text{ g/cm}^3$ ) and  $\text{Re}$  is the Reynolds number (dimensionless). For the range of shear stresses obtainable, the Reynolds number varies from  $0.02$  to  $54.8$ , indicating that the fluid flow through the chamber is laminar. Schlichting<sup>50</sup> gives an estimate of the entry length for plane Poiseuille flow as

$$l = (0.044)h \text{ Re}, \quad (7)$$

where  $l$  is the entrance length ( $\text{cm}$ ). For the maximum obtainable Reynold's number ( $54.8$ ) the entrance length is  $0.05 \text{ cm}$  which is very small compared to the effective length of the chamber ( $3.5 \text{ cm}$ ). Therefore, entry effects can be neglected and the flow is said to be fully developed and parabolic over nearly the entire length of the flow chamber. For a more complete description of flow chamber design and applications refer to the text edited by Frangos.<sup>51</sup>

### C. Experimental determination of point spread function

To experimentally determine the PSF one needs to optically section a point source. Fluorescent beads that were smaller than the resolution of the microscope were used as point sources. The use of fluorescent microspheres has proven to be a practical method by which to experimentally determine the PSF.<sup>27,28,39,42</sup> However, there are tradeoffs in deciding which bead size to use—very small beads are dim (small S/N) and bleach rapidly, while large beads are poorer approximations to a point source.<sup>52</sup> In fact, if the bead size is too large the observed data will correspond to an image convolved with the bead shape rather than with a point source.<sup>39</sup> A study was conducted by Preza *et al.*<sup>52</sup> to quantify the tradeoff between the quality of image reconstructions and the bead size used in the PSF measurement and they concluded that the diameter of the bead should be appreciably less than the first dark ring of the PSF (i.e., dark ring in the Airy disks). The diameter of the first dark ring is determined by using the standard microscope resolution equation. The resolution of an epifluorescent microscope is given by

$$\mathcal{R} = \frac{0.61 \lambda}{\text{NA}}, \quad (8)$$

where  $\lambda$  is the wavelength of the emitted fluorescence and  $\text{NA}$  is the numerical aperture of the objective lens. Thus, for a  $0.95 \text{ NA}$  and a Fura-2 emittance of  $510 \text{ nm}$ , the resolution

is  $0.33 \mu\text{m}$ . This gives an upper bound for the bead diameter. The study further concluded that the ideal bead diameter should be approximately 30% of  $\mathcal{R}$ ; this would result in a  $0.1 \mu\text{m}$  bead diameter. A bead size of  $0.1 \mu\text{m}$  was attempted, but the emitted image intensity was too dim to be measured with the SIT camera. As a consequence, we chose to use  $0.2 \mu\text{m}$  CML polystyrene latex beads loaded with a yellow-green fluorescent dye (Molecular Probes). The beads emit peak fluorescence at  $515 \text{ nm}$ , which is near the peak emission for Fura-2 bound to calcium ( $510 \text{ nm}$ ). The beads are purchased as a 2% solids solution; however, this is too high a concentration of beads. If the concentration of beads is too high, beads will be too close to one another such that the beads will aggregate and will not be surrounded by adequate amounts of background. As a result, the bead solution was diluted  $15\times$  using deionized distilled water.

A few drops of the diluted bead solution were placed onto a coverslip and the beads were allowed to dry on the coverslip. If the beads are allowed to stay in suspension they move around in the solution due to Brownian motion. This presents an intractable image registration problem when one attempts to stack the optical sections on each other to obtain a three dimensional volume data. Once the solution dried, the coverslip was attached to the flow chamber and are then optically sectioned using an excitation wavelength of  $440 \text{ nm}$ . The emission optics for the beads were identical to those for Fura-2 loaded cells. The image planes were serially acquired by stepwise movement of the objective via the  $z$ -axis stepper in a single direction to minimize the possibility of hysteresis effects in the focusing motor. In addition, there was no focus drift when observing beads for extended periods of time. There were typically ten beads in the field of view and all beads were optically equivalent. At each amount of defocus, four to eight video frames were averaged during acquisition to improve the S/N. Since the data measured will still be inherently of low intensity, especially at large amounts of defocus, one can further improve the S/N by superimposing several beads from each image plane and then averaging them. Finally, the image planes can be stacked together to form the three dimensional PSF. The beads did not photobleach significantly during the optical sectioning.

### D. Generation of computer phantoms

To test whether or not the deconvolution is being performed correctly and to determine the deconvolution algorithm's efficiency, 1D and 2D data sets were digitally fabricated. Although the 1D and 2D data sets are fabricated computer phantoms, they are not without an experimental basis or application. The 1D data set is similar to what is obtained from spectrographic data. In fact, one of the first applications of digital deconvolution was performed by Jansson in 1984 to deconvolve spectroscopy data.<sup>32</sup> The 2D data are modeled to reflect the intracellular ion measurements one may find in a cell. The ideal cell was assumed to be a circle with a concentric, circular nucleus. The gray level intensity of the nucleus was set higher than the cytoplasm ( $240$  vs  $205$ ). In addition, localized regions of increased intensity ( $230$  gray level) were scattered throughout the cytoplasm. The pixel sizes of the 1D and 2D data sets were  $1 \times 1 \times 32$



and  $1 \times 64 \times 64$ , respectively. The 1D and 2D computer phantoms are intentionally blurred using a digitally fabricated PSF, yielding a 1D and 2D blurred data set. These data sets were then deconvolved using the constrained, iterative regularization method and the results were compared to those obtained with a basic linear Wiener filter.

## E. Fluorescent beads

In addition to the computer phantoms, the deconvolution technique was tested on a real, three dimensional fluorescent specimen that has a known geometry prior to using the technique on endothelial cells. The same  $0.2 \mu\text{m}$  fluorescent latex beads (Molecular Probes) used in determining the PSF were used as the test specimens. Since the bead images were acquired with the video microscopy and digital imaging system, the images possess noise, as will digitized biological specimens, that is absent in the computer phantoms. After acquiring optical sections of the beads, the beads were deconvolved using the experimentally determined PSF. Deconvolving the acquired data with the experimentally determined PSF should result in a spherical fluorescent bead image in 3D.

## F. Preparation of endothelial cell monolayer

Bovine aortic endothelial cells (BAECs) were cultured in Dulbecco's Modified Eagle Medium (Gibco) supplemented with 10% fetal bovine serum (Hyclone), 1% glutamine (Gibco), 0.5% fungizone (Gibco), 25 mM HEPES buffer (Gibco), and 1% antibiotics containing 5 mg/ml penicillin, 5 mg/ml streptomycin, and 10 mg/ml neomycin (Gibco). The cells were cultured in T-25 flasks (Corning) and incubated at  $37^\circ\text{C}$  in an atmosphere of 5%  $\text{CO}_2$  and 95% humidified air. The culture medium was normally changed every three days. When confluent, the BAECs were passaged using 0.25% trypsin in 1:5000 EDTA (Gibco) and were seeded in T-25 flasks for subculturing at  $1 \times 10^6$  cells/flask or onto glass coverslips (#1, Corning) for experiments at  $1 \times 10^5$  cells/coverslip. The BAECs seeded on the coverslip were allowed to reach confluency and exhibit a cobblestone morphology<sup>53</sup> prior to actual experiments; a confluent monolayer is the physiological state of the cells in the vasculature. The intracellular calcium concentrations were measured in unstimulated BAECs (basal level calcium) and in BAECs stimulated with  $10 \mu\text{M}$  ATP and a  $1.4 \text{ dyn/cm}^2$  shear stress.

## G. Fura-2 loading and *in situ* calibration

To quantitate intracellular calcium concentrations, the BAECs were loaded with the calcium sensitive, fluorescent dye Fura-2.<sup>47,49,54,55</sup> Fura-2 is a ratiometric dye whose spectral properties change when the dye binds to free calcium. The excitation maximum of Fura-2 shifts from 380 nm to 340 nm as calcium concentration increases, as depicted in Fig. 4. Loading was accomplished by first incubating the BAECs at  $37^\circ\text{C}$  with  $20 \mu\text{M}$  Fura-2/AM (Molecular Probes), a cell permeable derivative of the dye. In this form, the dye is not fluorescent and will not bind free calcium. After loading for 30 minutes the BAECs were washed with HBSS twice to remove excess dye and incubated for another

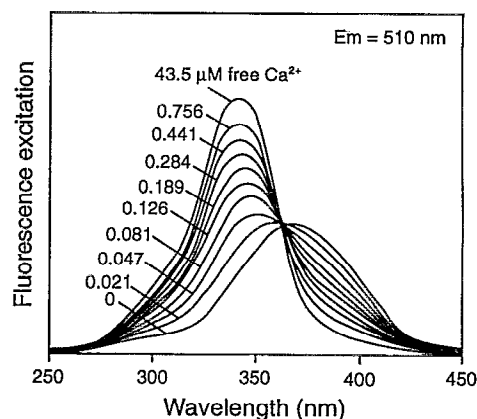


FIG. 4. Excitation spectra of Fura-2 as a function of  $[\text{Ca}^{2+}]$ . (Figure reprinted with permission from Molecular Probes.)

30 minutes to allow intracellular esterases to hydrolyze Fura-2/AM to Fura-2, the calcium binding form of the dye. In this form, the dye is fluorescent and is impermeable to intracellular and extracellular membranes. The coverslip with the Fura-2 preloaded BAECs was then mounted on the parallel plate flow chamber, placed on the microscope stage, and allowed to reach temperature and medium equilibrium.

The fluorescence intensity ratio ( $R$ ) of Fura-2 is related to free intracellular calcium concentration by the following equation<sup>55</sup>

$$[\text{Ca}^{2+}] = (\kappa_d)(\beta) \left( \frac{R - R_{\min}}{R_{\max} - R} \right), \quad (9)$$

where  $R$  is the ratio of background subtracted Fura-2 emission (510 nm) at 340 nm excitation to that at 380 nm excitation,  $R_{\min}$  is the ratio value at zero  $[\text{Ca}^{2+}]$ ,  $R_{\max}$  is the ratio value at saturating  $[\text{Ca}^{2+}]$ ,  $\kappa_d$  is the dissociation constant of Fura-2, and  $\beta$  is the ratio of background subtracted Fura-2 emission at 380 nm excitation and zero  $[\text{Ca}^{2+}]$  to that of background subtracted Fura-2 emission at 380 nm excitation and saturating  $[\text{Ca}^{2+}]$ . The parameters needed to relate  $R$  to  $[\text{Ca}^{2+}]$  were obtained by performing an *in situ* calibration using the calcium ionophore ionomycin (Calbiochem).<sup>56,57</sup> Briefly,  $R_{\max}$  was obtained by exposing Fura-2 loaded BAECs to HBSS (contains 1.3 mM  $\text{CaCl}_2$ ) and  $10 \mu\text{M}$  ionomycin.  $R_{\min}$  was obtained by exposing Fura-2 loaded BAECs to  $\text{Ca}^{2+}$ -free HBSS, 3 mM EGTA (Sigma), and  $2 \mu\text{M}$  ionomycin.  $\kappa_d$ , corrected for temperature ( $37^\circ\text{C}$ ) and ionic strength (149.8 nM), is 217.6 nM.  $R_{\max}$ ,  $R_{\min}$ , and  $\beta$  were found to be 2.3274, 0.1146, and 2.761, respectively. The *in situ* calibration curve relating  $R$  with pCa ( $\log_{10}[\text{Ca}^{2+}]$ ,  $[\text{Ca}^{2+}]$  in nM) is shown in Fig. 5. The BAECs did not photobleach significantly over the period of experiments performed (data not shown).

## H. Acquisition procedure and considerations

Fluorescent beads and Fura-2 loaded BAECs were prepared for imaging as discussed above. Prior to any experimental runs, the excitation lamp was adjusted to yield the most homogeneous distribution of intensities of a Fura-2 free



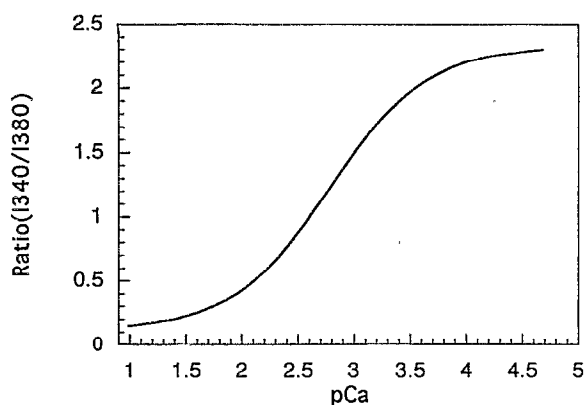


FIG. 5. *In situ* calibration curve of Fura-2. The calibration curve relates the ratio value obtained from digital image processing to pCa ( $\log_{10}[\text{Ca}^{2+}]$ ,  $[\text{Ca}^{2+}]$  in nM) according to Eq. (9).  $\kappa_d = 217.6$  for  $T = 37^\circ\text{C}$  and  $I = 149.8$  nM.  $R_{\text{max}} = 2.3274$ .  $R_{\text{min}} = 0.1146$ .  $\beta = 2.761$ .

acid solution as measured by a gray level histogram. In addition, the microscope's field diaphragm was closed to its minimum aperture to reduce unwanted photobleaching of specimens. Acquisition of images was accomplished by using RatioTool™ (Inovision), a window based program for the acquisition and processing of fluorescence ratio images as well as single wavelength fluorescence images. The software provides interfaces for controlling peripheral devices (camera, filter wheel, shutter, z-axis stepper motor) synchronously with the IC-300 video hardware. The software was typically set to average four or eight frames per image sample to increase the S/N. In addition, an 11 frame camera delay was incorporated to compensate for the SIT camera lag. A sequence file was used by the software to carry out the optical sectioning; the user must decide beforehand the upper and lower sectioning limits as well as the stepping interval.

There are several limits which set the bounds for the increment size in the  $z$  direction (focal axis) during optical sectioning. The first is the microscope's depth of field. The depth of field is the physical distance along the focal axis through which the specimen observed is in focus at the image plane.<sup>40</sup> In other words, it is the distance that a single point object can be moved in the focal direction before the image changes. This is the lower increment constraint, for one does not want to take smaller increments if the images are not changing. The depth of field is given by

$$\mathcal{D} = \frac{\lambda}{4n \sin^2(\theta/2)}, \quad (10)$$

where  $\mathcal{D}$  is the depth of field expressed in length units,  $\lambda$  is the wavelength of illumination expressed in length units,  $n$  is the refractive index of the immersion medium ( $= 1.0$  for air), and  $\theta$  is the half-angle of the cone of light that is captured by the objective lens and is given by

$$\theta = \sin^{-1}(\text{NA}/n). \quad (11)$$

Substituting for the known values, the depth of field for the 510 nm Fura-2 emission is  $0.37 \mu\text{m}$ . Thus, we do not want to theoretically choose increments smaller than  $0.37 \mu\text{m}$  during optical sectioning. However, it has been shown that one is

able to use section increments below this theoretical limit with fluorescence microscopy; this phenomenon is referred to as super-resolution.<sup>40,41</sup> Another limit is image storage. One does not want to choose too small of increments such that the number of images recorded will not fit into computer storage. On the other hand, too large increments cause loss of data resolution in the image volume. Typically an increment of  $0.5\text{--}1.0 \mu\text{m}$  was used.

The first images acquired during the acquisition were the background images. Since our cells and flow media do not autofluoresce significantly at 340 or 380 nm, the background images consisted merely of the SIT camera's dark current. For the BAECs, a 340 nm and a 380 nm image was acquired at each focal position defined in the sequence file. Typically,  $\sim 1.5$  s is required to record and write to disk a ratio pair (image size  $256 \times 256$  pixels). For the beads, a single 440 nm image was recorded at each focal position. After acquisition, the images were digitally processed off-line, as shown schematically in Fig. 6. The majority of the processing can be done on-line during acquisition; however, this would increase the acquisition time. Typically the raw images were background subtracted to remove the camera's dark current, scaled from a 3:4 video format to a 1:1 format, and thresholded to remove extraneous noise or artifacts. The processed 340 nm and 380 nm images could then be ratioed to obtain the "blurred" ratio images. In addition, the processed 340 nm and 380 nm images were deconvolved using a constrained, iterative regularization deconvolution algorithm (discussed below in Sec. IV). The deconvolved 340 nm and 380 nm images were then ratioed to yield the deconvolved ratio images. The data can be viewed as a 3D data set using volume rendering (see below in Sec. III I), as 2D data sets as individual slices, or as 1D vector profiles. In addition, to quantitate the intracellular ion concentrations, the gray level intensity data in the ratio images were mapped to concentration units by utilizing the calibration curve discussed above in Sec. III G.

## I. Scientific visualization

Sun Vision's interactive, 3D volume rendering software, SunVoxel™, was used to generate 3D volumetric images of the acquired bead and cell data. This software has also been used by Willis *et al.* to view 3D reconstructions of rat hippocampal neurons.<sup>58</sup> The acquired data was 3D reconstructed into a 3D volumetric data set by stacking the 2D slices and interpolating between them.<sup>59</sup> The software allows digital, non-destructive orthogonal and oblique slicing of the volumetric data. The data sets can be either viewed using texture mapping, where volume data is displayed on exposed volume surfaces, ray casting, where rays are spawned along the viewing vector of the volume and the maximum value encountered by the vector is displayed, or transparent surfaces, where the volume is displayed as a semitransparent surface using user defined substance classification, pseudocolor, and opacity values. Since the  $XY$  and  $Z$  pixel resolutions of the acquired images differ ( $0.54 \mu\text{m}/\text{pixel}$  vs  $\{0.37 + \text{optical sectioning step increment}\} \mu\text{m}/\text{pixel}$ , respectively) the aspect ratio of the  $Z$  axis, which maps model space to screen space,

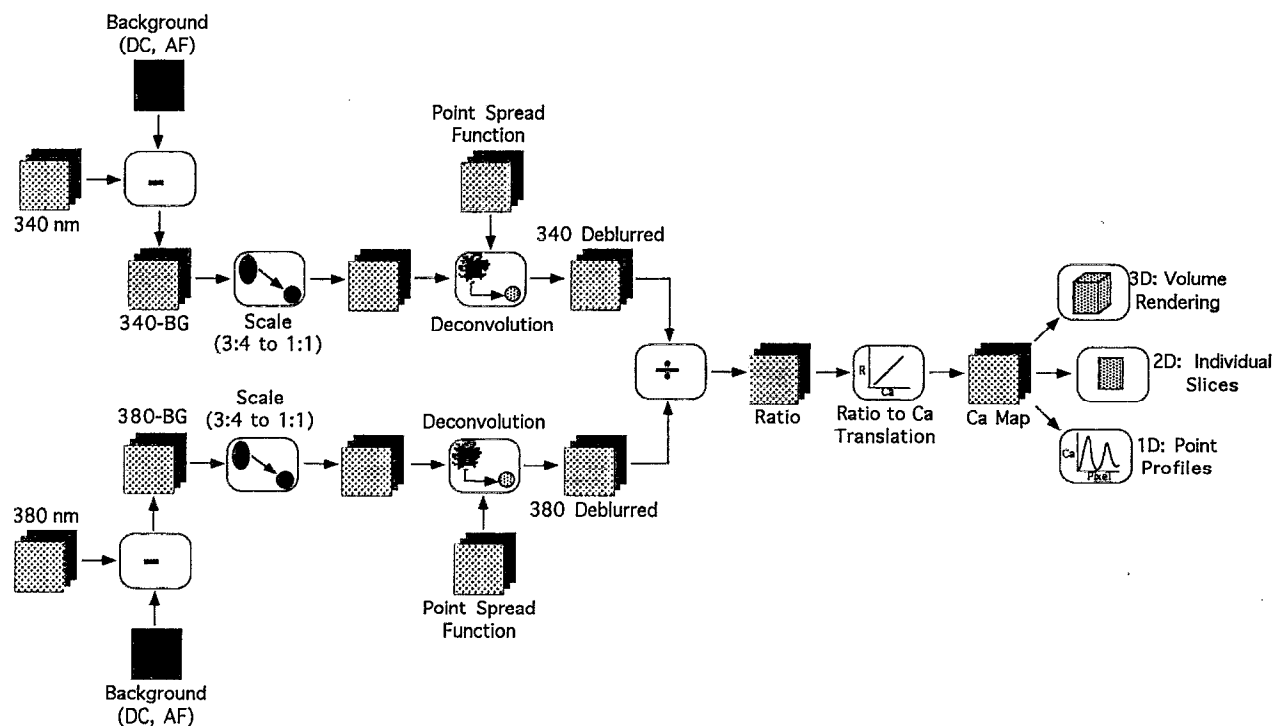


FIG. 6. Flow diagram of digital processing of the acquired data.

was set so that all three coordinate axes have the same visual resolution (i.e., a sphere will appear as a sphere rather than an ellipsoid).

#### IV. DECONVOLUTION ALGORITHM

##### A. Theory and mathematics

As previously stated, the simplest method by which to obtain the true image from the observed image would be straightforward deconvolution via an inverse filter as in Eq. (4). However, this deconvolution process is ill-conditioned or ill-posed; that is, it is extremely sensitive to the noise that is present in real images. The noise in the PSF is usually of low spatial frequency; hence, taking the inverse with small values greatly increases the noise present in the solution for the true image and in the extreme case (but highly probable) of inverting by zero, it increases the noise to a value of  $\infty$ . Stated differently, for values of low spatial frequency, the PSF is singular and cannot be simply inverted. An optimal linear filter can be obtained by adding a parameter,  $\lambda$ , to the OTF in the denominator of Eq. (4) so that one does not invert by zero.<sup>22,24,26</sup> The  $\lambda$  can either be set as a constant or as a function of S/N. This inverse filter is known as a Wiener filter and is given by

$$I = (O) \left( \frac{\text{OTF}}{\text{OTF}^2 + \lambda} \right). \quad (12)$$

However, the Wiener filter still distorts or obscures weak features in an image due to the fact it causes negative “ripples” to build up around strong features.<sup>22</sup> This oscillatory behavior is distinctive of a linear filter.

Therefore, another method must be implemented to successfully deconvolute the data without introducing additional distortions due to noise. The algorithm chosen is a regularization method with nonnegative constraints first proposed by Butler *et al.*<sup>60</sup> and later extended by Carrington<sup>38,61</sup> and Carrington *et al.*<sup>21,35</sup> whose solution lies in a closed, convex set. This method was chosen for its robustness, strong mathematical basis, relatively fast and efficient convergence, its ability to guarantee a solution mathematically, its ability to constrain the problem with *a priori* information, and its proven effectiveness over a whole range of fluorescent images. The method states that the true (deblurred) images  $i$  are those which minimize

$$\min_{i \geq 0} [\|o - \text{psf} \otimes i\|^2 + \alpha \|i\|_2^2], \quad (13)$$

where  $\alpha$  is the regularization parameter. A nonnegativity constraint is incorporated in the minimization by constraining the dye density in the solution for  $i$  to be strictly positive. Although negative densities are mathematically possible (optical density is a complex number with nonzero real and imaginary parts) they are physically meaningless. Hence, advantage is taken of this fact to constrain the solution for  $i$ . This gives the algorithm greater stability by removing oscillations typical in unconstrained solutions. The first term in the minimization, the residuals, measures how well  $i$  fits the data. The second term, the energy of  $i$ , measures the smoothness of  $i$ . In the absence of noise,  $\alpha$  would be set to zero and  $i$  would fit the data exactly. However, in the presence of noise the solution becomes too sensitive to the noise and begins to oscillate. On the other hand, if  $\alpha$  is chosen to be too large the second term will average out any sensitivity and

yield a flat distribution. The proper choice of  $\alpha$  balances the solution fit and smoothness. Carrington<sup>38</sup> proposes one way of choosing  $\alpha$  is so that the residual term is slightly larger than an estimate of the noise variance. He has shown that this choice of  $\alpha$  regularizes the problem. As a consequence, the noisier the observed image data are, the larger the choice of  $\alpha$  should be.

Butler *et al.*, Carrington, and Carrington *et al.* have proposed a reliable and quite elegant algorithm for performing the minimization in Eq. (13) and have proved that the algorithm mathematically converges to a minimum.<sup>35,38,60,61</sup> They use methods from convex analysis to reduce the infinite dimensional constrained minimization in Eq. (13) to a finite dimensional unconstrained minimization problem. The related minimization problem belongs to a closed convex set and, thus, has a unique minimum. They show that the  $i$  that minimizes Eq. (13) has the form

$$i = \max(0, \text{psf} \cdot c), \quad (14)$$

where  $c$  is found by minimizing

$$\psi = \int \int \int_{(\text{psf} \cdot c) \geq 0} (\text{psf} \cdot c)^2 + \alpha \|c\|^2 - o \cdot c. \quad (15)$$

The gradient can be determined as

$$\psi' = \int \int \int_{(\text{psf} \cdot c) \geq 0} [\text{psf}(\text{psf} \cdot c)] + \alpha c - o \quad (16)$$

and the Hessian is

$$\psi'' = \int \int \int_{(\text{psf} \cdot c) \geq 0} [(\text{psf})(\text{psf})] + \alpha. \quad (17)$$

The integration in Eqs. (15)–(17) is not integrated over all space, but only over the domain where the true image estimate in Eq. (14) is positive. This reflects the nonnegativity constraint. Because  $\psi$  is strictly convex and is twice differentiable a number of numerical minimization methods can be employed to reach a solution. Although a conjugate gradient method would normally be preferred, we elected to use a variation of Newton's method proposed by Carrington and Fogarty.<sup>35</sup> The advantage of Newton's method over a conjugate gradient method is that a line search is not required, which can be too time consuming for the large data sets normally acquired in 3D imaging. Since the assumption has been made that the optical/imaging system is space invariant, we can calculate the convolutions and matrix inversion required for Newton's methods in Fourier space, thereby reducing the convolutions and inversions to multiplication and division. This greatly increases the computational speed of the algorithm (by  $\sim 500$  times). In Fourier space, Eqs. (16) and (17) become, respectively,

$$\mathcal{F}[\psi'] = \text{OTF} \mathcal{P}[(\text{OTF}^*)(C)] - O + \alpha C \quad (18)$$

and

$$\mathcal{F}[\psi''] = (\text{OTF})(\text{OTF}^*) + \alpha + \lambda, \quad (19)$$

where  $\mathcal{F}[\ ]$  represent Fourier transforms,  $\lambda$  is the quasi-Newton parameter (normally set to 0.1),  $*$  represents the complex conjugate, and

$$\begin{aligned} \mathcal{P}[(\text{OTF}^*)(C)] \\ = \begin{cases} (\text{OTF}^*)(C) & \text{if } \mathcal{F}^{-1}[(\text{OTF}^*)(C)] \geq 0, \\ 0 & \text{if } \mathcal{F}^{-1}[(\text{OTF}^*)(C)] < 0. \end{cases} \end{aligned} \quad (20)$$

The iteration used in the Newton method for solving  $c$  is

$$\begin{aligned} c^{k+1} &= c^k - \psi' / \psi'' \\ &= \mathcal{F}^{-1} \left[ \frac{(\text{OTF}) \mathcal{P}[(\text{OTF}^*)(C)] - O + \alpha C}{(\text{OTF})(\text{OTF}^*) + \alpha + \lambda} \right], \\ c^0 &= 0. \end{aligned} \quad (21)$$

The iteration on  $c$  is terminated when a defined number of maximum iterations is reached. Once a solution for  $c$  is reached such that Eq. (15) is minimized, the deblurred image date,  $i$ , is determined from Eq. (14).

To determine the "goodness of fit" the  $R$ -factor is computed. The theory behind the  $R$ -factor is if the solution estimate for  $i$  is correct then  $i$  convolved with  $\text{psf}$  should yield the observed data,  $o$ . The  $R$ -factor, or refinement factor, is the residual between the observed data and the solution image convolved with the PSF and is given by

$$R\text{-factor} = \frac{\|\text{psf} \otimes i - o\|}{\|o\|}. \quad (22)$$

A value of zero represents the best fit.

## B. Algorithm implementation

The above algorithm was programmed in C++ and was implemented on the Sun IPX. Included in the program are links to Inovision's digital imaging software/hardware libraries for inputting and outputting the image pixel gray levels. The majority of the processing time is consumed by the 3D Fourier transforms that are used for the convolutions and matrix inversions. The processing time increases with larger image volumes since the Fourier transform processing time increases proportionally to  $(N)(\log N)$ , where  $N$  is the number of voxels in an image volume. For instance, a  $1 \times 128 \times 128$  image ( $N=16\,394$ ), a  $32 \times 64 \times 64$  image ( $N=131\,072$ ), and a  $64 \times 128 \times 128$  image ( $N=1\,048\,576$ ) require 1.0, 15.8, and 120.3 minutes of run time (real time rather than CPU time) to complete 50 iterations of the deconvolution algorithm. We would eventually like to be able to deconvolve data sets that are  $64 \times 480 \times 512$  ( $N=15\,728\,640$ ) in a reasonable amount of time (minutes rather than days). Willis *et al.* also have used a Sun SPARC workstation for 3D deconvolution.<sup>58</sup> They report a 2 day processing time for 600 iterations of their deconvolution algorithm on a  $128 \times 480 \times 512$  image ( $N=31\,457\,280$ ). In addition, they speculate that the addition of a high speed vector processor will decrease the processing time to a satisfactory 18 minutes. Investigation into methods by which to decrease our run times is in progress.

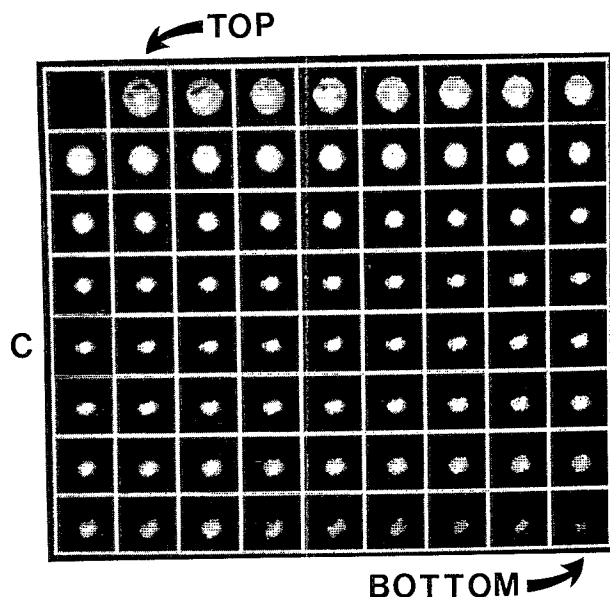


FIG. 7. Mosaic of a series of 2D slices of the PSF. A  $0.2\ \mu\text{m}$  fluorescent microsphere was used as the PSF model and was optically sectioned with a  $0.2\ \mu\text{m}$  stepping interval. The optical series ranges from  $+7\ \mu\text{m}$  (top) to  $-7\ \mu\text{m}$  (bottom). The central optical slice is outlined in yellow and is denoted by C. The optical series is incremented by  $+0.2\ \mu\text{m}$ , traversing right to left, above the central optical slice and is decremented by  $-0.2\ \mu\text{m}$ , traversing left to right, below the central optical slice. Note the formation of Airy disks at extended amounts of defocus below the central optical slice.

## V. RESULTS AND DISCUSSION

### A. Experimental PSF

Fluorescent microspheres were used to model the PSF as discussed in Sec. III. A mosaic of individual 2D slices acquired from a bead is shown in Fig. 7. There is a  $0.2\ \mu\text{m}$  step between each slice and the optical series shown ranges from  $+7$  to  $-7\ \mu\text{m}$ . The mean intensity of each slice of the PSF as a function of defocus distance is shown in Fig. 8. These figures imply that a point source significantly contributes to the fluorescence signal  $9\ \mu\text{m}$  above and  $8\ \mu\text{m}$  below the in-focus focal plane. The fluorescence signal contributions

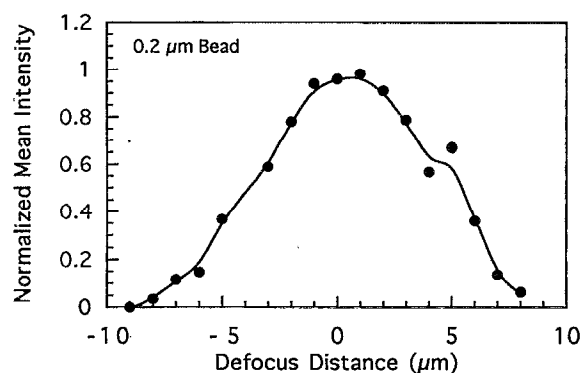


FIG. 8. Mean intensity of PSF XY sections vs defocus distance. Positive and negative defocus values denote optical slices above and below the central optical slice (0), respectively. The intensity values are normalized with respect to the largest mean intensity. ● denotes actual data and — denotes a smooth curve fit.

above  $9\ \mu\text{m}$  and below  $8\ \mu\text{m}$  are assumed negligible since the detected signal decreased to background signal values. Hence, the acquired PSF data are truncated to a range of  $9$  to  $-8\ \mu\text{m}$ . In addition, the PSF is not circularly symmetric in the XY plane. This is most probably due to residual spherical aberrations.<sup>28,40</sup> Since every imaged bead exhibited the same asymmetry in the XY plane, it was assumed that this is a characteristic of the imaging system and, as a result, the PSF data was not radially averaged before its use in the deconvolution algorithm. Furthermore, the distinctive Airy disks can be observed in Fig. 7. However, the Airy disks form only above the in-focus focal plane and not below. Hence, the PSF is asymmetric in the focal direction (Z). The asymmetry above and below the in-focus focal plane can be corrected by increasing or decreasing the refractive index of the immersion oil used with oil immersion objective lenses or by using objective lenses that have correction collars.<sup>28,29</sup> The objective lens used in this study was not an oil immersion lens, but it does have a correction collar. Extreme changes in the correction collar did make the PSF more symmetric (data not shown); however, these changes made it impossible to completely optical section the biological specimens under interests. As a result, the PSF shown in Fig. 7 was used since the experimental conditions used to measure the PSF must match those used to measure the intracellular ions in cells. Since light scattering can alter a PSF's shape, microspheres measured on dry coverslips were compared to those measured on coverslips and surrounded by cell culture media. There is no significant difference in the PSF measured without and in the presence of cell culture media (data not shown). In support, Blumenfeld *et al.* have shown that light scattering due to cell culture media and cell cytoplasm did not change the measured PSF when compared to a PSF measured on a dry coverslip.<sup>42</sup> Consequently, microspheres on dry coverslips can be used to model the PSF.

The PSF results obtained show that the experimentally determined PSF deviates greatly from what diffraction theory dictates (symmetric PSF in all three coordinate directions) and reaffirms the need to determine the PSF under experimental conditions. In addition, a point source contributes a significant amount of fluorescence signal in the focal direction and spreads out a significant amount in the XY plane.

### B. 1D and 2D deconvolution of computer phantoms

A 1D computer phantom was intentionally blurred with a model PSF and then deblurred using a linear Wiener filter and the constrained, iterative regularization deconvolution algorithm. Figure 9 shows the 1D computer phantom results. The  $R$ -factors for the Wiener filter ( $\lambda=0.1$ ) and the constrained, iterative regularization deconvolution algorithm are  $0.04$  and  $3.6 \times 10^{-5}$ , respectively. The constrained, iterative regularization deconvolution algorithm removes the out-of-focus information and reconstructs the true function whereas the linear Wiener filter does not remove all the out-of-focus information and the magnitude of the peaks in the Wiener function are lower than the true function. In addition, the low intensity "tails" observed in the Wiener filtered function are

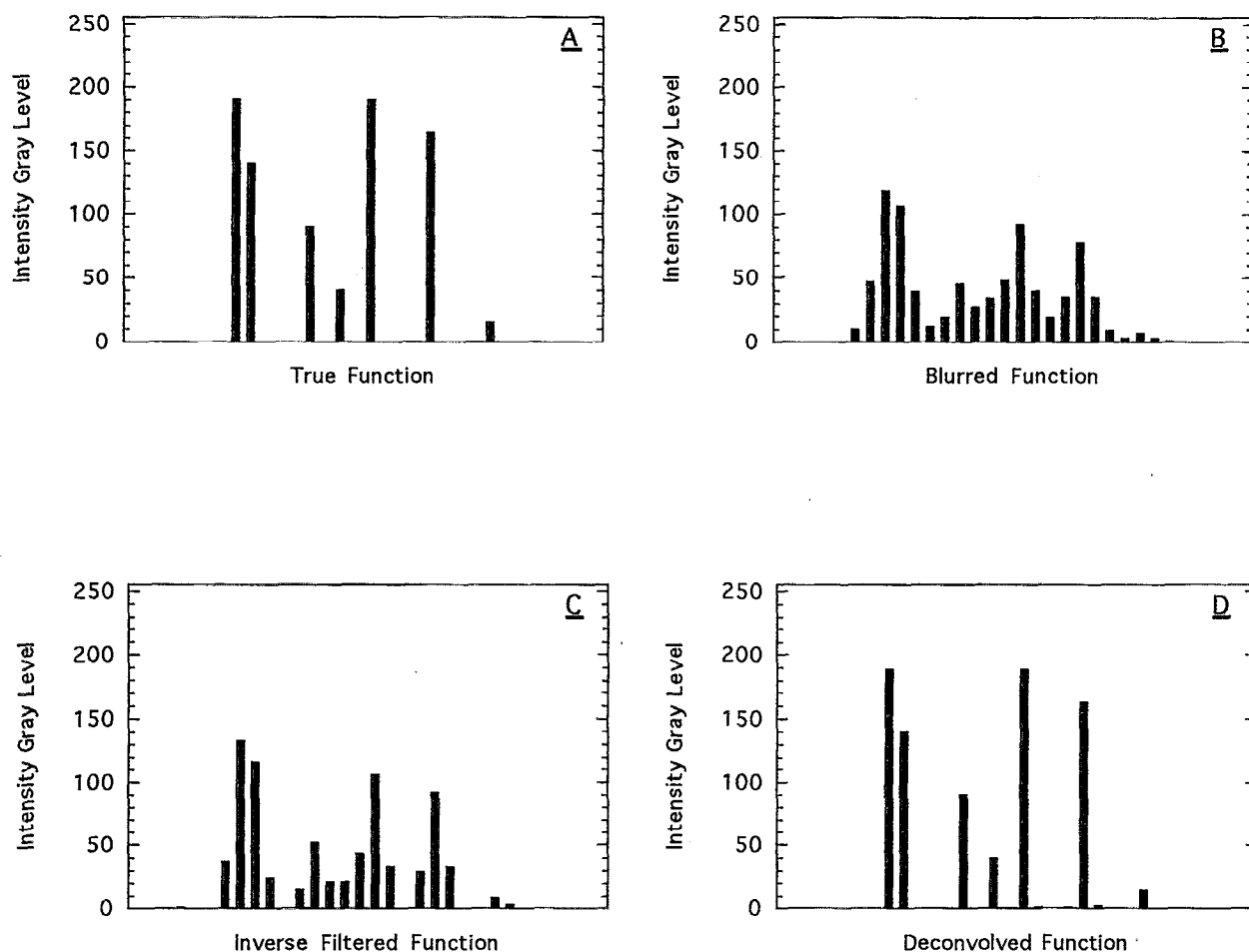


FIG. 9. Results from a 1D computer phantom. The true function (A) was intentionally blurred with a model PSF to yield a blurred function (B). The blurred function underwent image restoration with a Wiener filter (C) and a constrained, iterative deconvolution algorithm (D). Parameters for the deconvolution algorithm were 50 iterations and  $\alpha=0.0001$ . The  $R$ -factor for the Wiener filtered and deconvolved functions is 0.04 and  $3.6 \times 10^{-5}$ , respectively.

removed by the non-negativity constraint in the deconvolution algorithm.

The regularization parameter ( $\alpha$ ) and the number of iterations used for deconvolving the 1D blurred phantom are 0.0001 and 15, respectively. Figure 10 shows the dependency of iteration number and  $\alpha$  on the efficiency ( $R$ -factor) of the

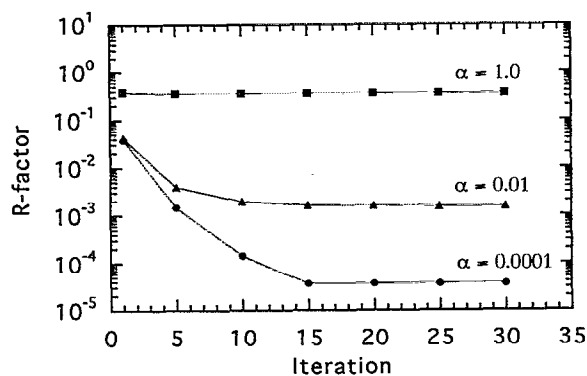


FIG. 10. Efficiency of the deconvolution restoration method as a function of  $\alpha$  and the number of iterations. Values were obtained using the 1D computer phantom.

deconvolution algorithm in reconstructing the true function. The algorithm performs the majority of the reconstruction in the first 10 iterations for the 1D case. More iterations are required for increased dimensionality. In addition, Fig. 10 demonstrates that if  $\alpha$  is increased too large the deconvolution algorithm averages out any sensitivity and yields a flat refinement profile.

In addition to the 1D computer phantom, a 2D computer phantom was tested. Figure 11 shows the 2D images. The colors on the intensity bar represent the gray level magnitudes. The total pixel area of the true, blurred, Wiener filtered, and deconvolved images are 489, 705, 725, and 552, respectively. The Wiener filtered image has lower gray level magnitudes and is spread out more (larger pixel area) than the true image. On the other hand, the deconvolved image is an excellent reconstruction of the true image. The  $R$ -factors for the Wiener filtered and deconvolved images ( $\alpha=0.001$  and 100 iterations) are 0.01 and  $8 \times 10^{-6}$ , respectively.

The results from the computer phantoms show that the deconvolution algorithm does appreciably better in reconstructing true data from blurred data than does a Wiener filter. This is due to both the nonlinear nature of the algorithm and the nonnegativity constraint incorporated in the algo-

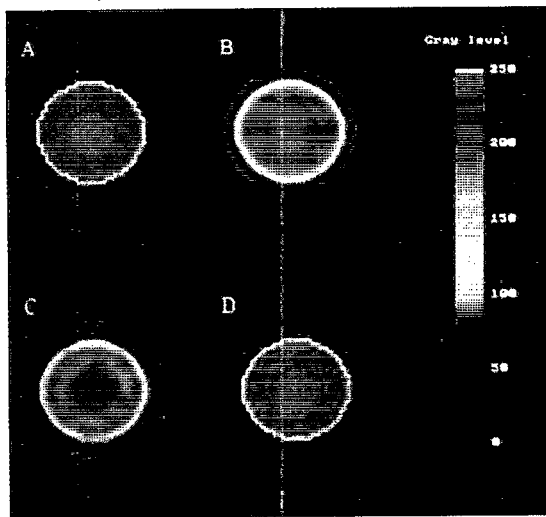


FIG. 11. Results from a 2D computer phantom. The true image (A) was intentionally blurred with a model PSF to yield a blurred image (B). The blurred image underwent image restoration with a Wiener filter (C) and a constrained, iterative deconvolution algorithm (D). Parameters for the deconvolution algorithm were 100 iterations and  $\alpha=0.01$ . The  $R$ -factor for the Wiener filtered and deconvolved functions is 0.01 and  $8 \times 10^{-6}$ , respectively. The color bar represents the gray level intensity.

rithm. In addition, there are only two parameters that have to be set by the user:  $\alpha$  and the number of iterations. The refinement for the deconvolution algorithm can be improved by fine tuning the choice of  $\alpha$  and the number of iterations. However, exact choices for these parameters are not needed. The value of  $\alpha$  does not affect the  $R$ -factor drastically as long as the correct order of magnitude is chosen. For instance, no significant change is observed in the 2D results if  $\alpha$  is changed from 0.001 to 0.005. This is due in part to the fact the gray levels are all integers; any change in refinement is lost during rounding off to integer values.

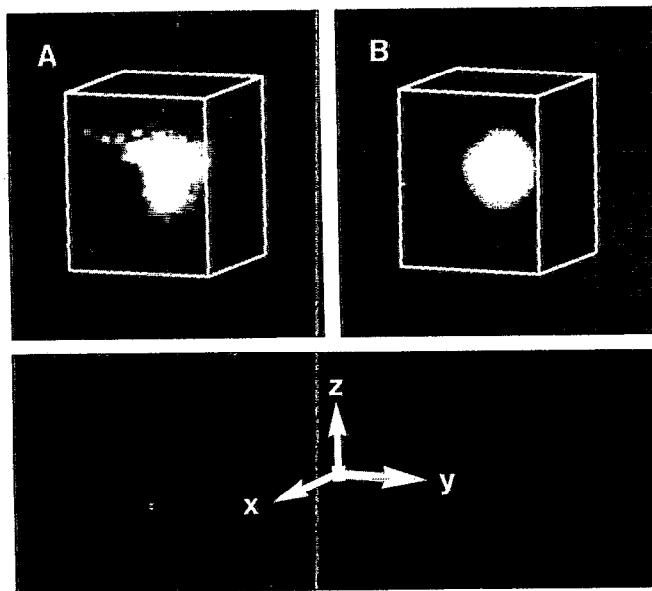


FIG. 12. Volume rendered  $0.2 \mu\text{m}$  fluorescent microsphere prior to (A) and after (B) deconvolution.

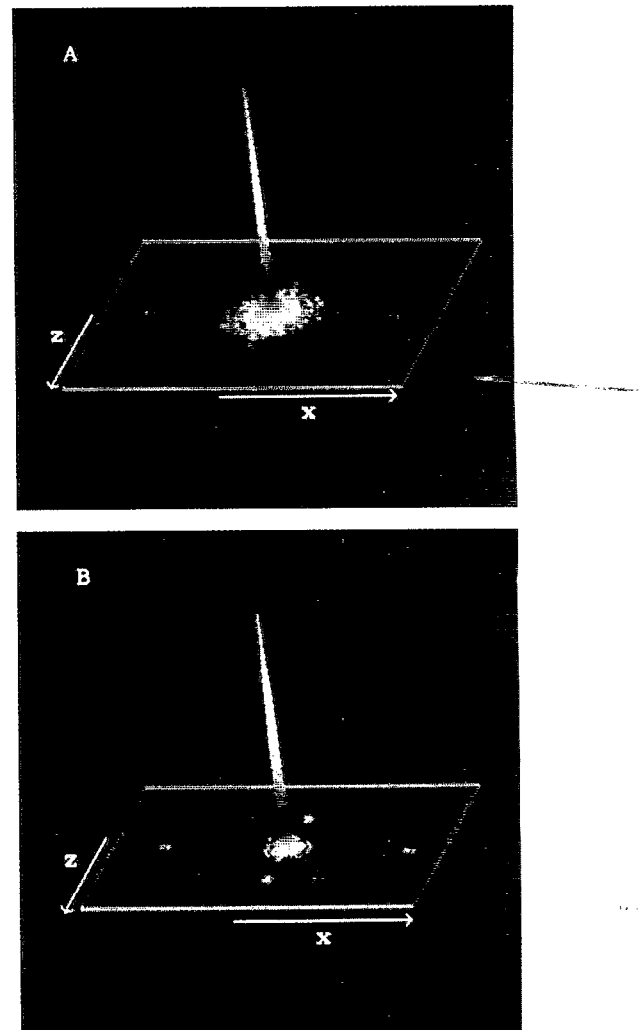


FIG. 13. 2D OTFs of the XZ sections shown in Fig. 12. Intensity is plotted on the vertical axis. (A) is the observed 2D OTF and (B) is the deconvolved 2D OTF. The color sequence purple-blue-green-yellow-orange-red-white denotes low to high OTF values.

### C. 3D deconvolution of fluorescent bead

Fluorescent microspheres were used to test the restoration algorithm on actual fluorescent specimens prior to use on biological specimens. Figure 12 shows a volume rendered  $0.2 \mu\text{m}$  bead prior to and after restoration with 25 iterations of the deconvolution algorithm ( $\alpha=0.1$ ). The asymmetry in the focal direction is quite evident in Fig. 12(A). The conical region above the in-focus focal plane is composed of the Airy disks stacked on top of each other. When deconvolved the asymmetry in all three coordinates is removed and the reconstructed image obtained is a sphere, shown in Fig. 12(B). This data set exhibits the magnitude of the out-of-focus information problem and how far from ideality a microscopy and digital imaging system can be. The specimen that is optically sectioned is a sphere. What is observed, however, is not a sphere but a distorted image that resembles an umbrella turned inside out. Only by applying deconvolution can the true image be restored, Fig. 12(B). The effectiveness of the restoration method can be further observed by

determining the 2D Fourier transforms of Figs. 12(A) and 12(B). The 2D Fourier transforms of the XZ sections are shown in Fig. 13 with intensity plotted on the vertical axis. Since the imaged beads are the same beads used to model the PSF, the 2D Fourier transform of the bead images can be referred to as the 2D OTFs. The colors on the intensity bar represent the gray level magnitude corresponding to the 2D OTF values (i.e., the maximum OTF value was mapped to 255 and all other values were linearly mapped such that a zero OTF value was mapped to 0). The observed 2D OTF in Figure 13(A) shows the existence of data far from the center and the existence of sloping "tails" (pseudocolored purple). These are due to the presence of the out-of-focus information. On the other hand, the deconvolution method has removed the out-of-focus information and placed the information into its proper place. This is evidenced by the disappearance of the "tails" and data far from the center. The 3D fluorescent bead data has shown that the restoration method works well in restoring a fluorescent object in the presence of noise. More specifically, the method removes the out-of-focus information from observed fluorescent specimens to obtain a restored true image of a fluorescent specimen.

#### D. Deconvolution of Fura-2 loaded BAECs

Confluent monolayers of BAECs were cultured, pre-loaded with Fura-2, and optically sectioned as discussed in Sec. III. The BAECs were observed under quiescent (HBSS, 0 dyn/cm<sup>2</sup>) and stimulatory (HBSS+10  $\mu$ M ATP, 1.4 dyn/cm<sup>2</sup>) conditions. A 256 $\times$ 256 pixel region of interest was chosen to bracket cells of interests in the monolayer. For deconvolution, a single cell was chosen and was centered in a 128 $\times$ 128 pixel region of interest after background subtraction and scaling. The BAECs were optically sectioned into 81 slices with a defocus stepping increment of 1  $\mu$ m. This resulted in a total section thickness ranging from +40 to -40  $\mu$ m. In addition, each slice has a 0.37  $\mu$ m thickness (depth of field). It required a total of 6.4 minutes to acquire 81 ratio pairs (340 and 380 nm images) of a 256 $\times$ 256 pixel region on interest. Each of the 81 incremental steps involved the following sequence of events: translate focal plane by the defocus distance, rotate filter wheel to 340 nm, open the shutter, 11 frame lag delay, average 4 frames for acquisition, close shutter, rotate filter wheel to 380 nm, open the shutter, 11 frame lag delay, average 4 frames for acquisition, close shutter. Of the total elapsed time, the cells are only exposed to excitation light for 2.7 minutes (42% of the elapsed time). The cells do not photobleach within this time frame.

Because of the time required for optical sectioning, one can only acquire 3D data during periods of sustained steady-state conditions. To determine the steady-state regions a 2D temporal study was first conducted. Figure 14 shows the average results of 65 BAECs. The [Ca<sup>2+</sup>] response of the BAECs was measured under basal conditions (region A), shear stress alone (region B), shear stress and 10  $\mu$ M ATP (region C), and removal of ATP (region D). There was no significant change in [Ca<sup>2+</sup>] once shear stress alone was applied; the [Ca<sup>2+</sup>] remained at 80 nM. However, once ATP was introduced, there was an initial 310 nM spike and then a

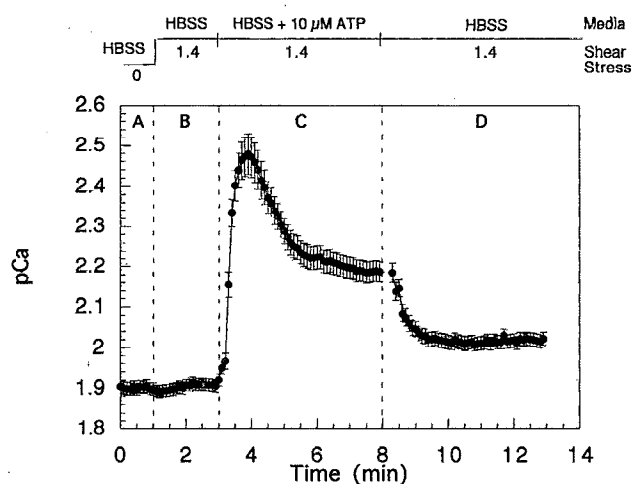


FIG. 14. Average response of BAECs to ATP and shear stress stimulation. Region A corresponds to no flow and no stimulation conditions. Region B corresponds to an applied 1.4 dyn/cm<sup>2</sup> shear stress, but no stimulation. Region C corresponds to an applied 1.4 dyn/cm<sup>2</sup> shear stress and 10  $\mu$ M ATP stimulation. Region D corresponds to a washing phase to remove the ATP under a 1.4 dyn/cm<sup>2</sup> shear stress. Results represent the mean $\pm$ SEM of 65 individual BAECs.

gradual decrease to a sustained plateau of 164 nM. The sustained elevated plateau remains until the ATP is removed from the extracellular media. Once the ATP is removed the [Ca<sup>2+</sup>] decreases to 111 nM, which is slightly elevated above basal level. The ATP response and its implications have been well characterized by others.<sup>12,13,62,63</sup> The reader is urged to refer to the provided references since the focus of this paper is to discuss the application of the 3D technique rather than to discuss the signal transduction of ATP stimulation. We elected to collect 3D data during the basal region (unstimulated) and during the elevated plateau in region C (stimulated).

The raw 340 and 380 nm images for the stimulated and unstimulated data sets were deconvolved with the experimentally determined PSF using 50 iterations and  $\alpha=0.008$ . The raw data size utilized in the deconvolution program was 128 $\times$ 256 $\times$ 256 (8 388 608 voxels). This is larger than the actual data (81 $\times$ 128 $\times$ 128; 1 327 104 voxels) because zero padding is needed for the FFT algorithm utilized by the program. It required approximately one day to deconvolve each data set under these conditions. The *R*-factor for the unstimulated 340 nm and 380 nm 3D data sets were 0.0693 and 0.0683, respectively. Likewise, the *R*-factor for the stimulated 340 and 380 nm 3D data sets were 0.0491 and 0.0650.

Figure 15 shows the raw and deconvolved 340 and 380 nm images of the central slice of an unstimulated BAEC (basal level). One can visually see how the deconvolution algorithm removes the majority of the out-of-focus light present in the raw images. In addition, there is increased clarity of the cell in the deconvolved images. Comparing Figs. 15(A) and 15(B), there is a 25% decrease in the 340 nm integrated intensity (a measure of the quantity of light). Similarly, when comparing Figs. 15(C) and 15(D), there is a 27% decrease in the 380 nm integrated intensity. The edges outlining a square in the deconvolved images [Figs. 15(B)



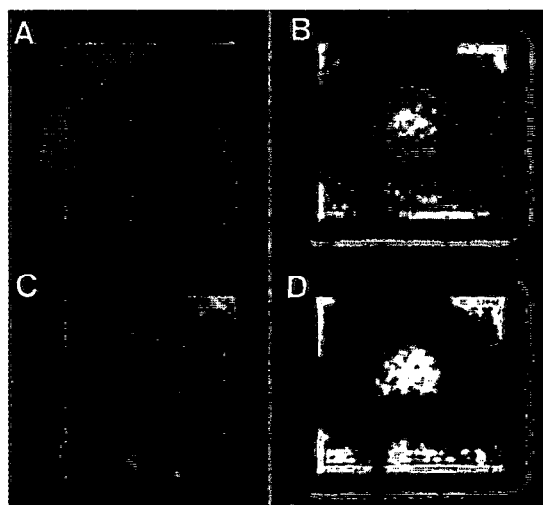


FIG. 15. Single wavelength images of the central optical slice of an unstimulated BAEC. Shown are the 340 nm raw (A) and deconvolved (B) images as well as the 380 nm raw (C) and deconvolved (D) images.

and 15(D)] are an artifact due to a discontinuity at the raw image and zero padding boundaries; future work will include smoothly rolling the raw image intensities to zero to remove the discontinuity. In addition to the integrated intensity, the area of the cell decreases by 63% in both the 340 nm and 380 nm images. Waybill *et al.* likewise observed a decrease in integrated intensity and increased image sharpness when deconvolving Fura-2 loaded rat hepatocytes using a nearest-neighbor deconvolution algorithm.<sup>64</sup> Yelamarty & Cheung and Yelamarty *et al.* have also observed the same trends in Fura-2 loaded human erythroblasts and rat hepatocytes.<sup>27,28</sup>

Figure 16 shows the central slice of a raw and deconvolved BAEC under unstimulated and stimulated conditions.

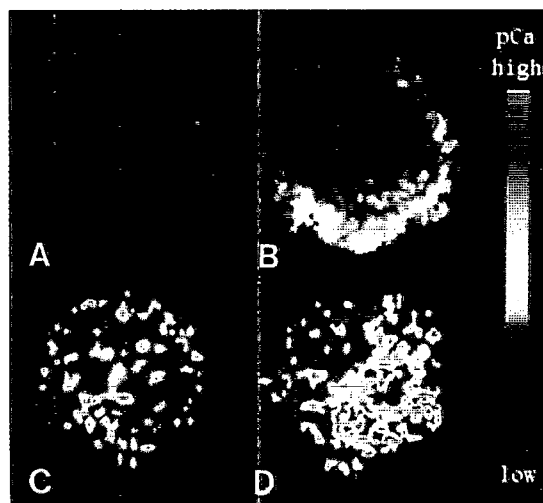


FIG. 16.  $[Ca^{2+}]$  distributions of the central optical slice of a BAEC under stimulated (ATP & shear stress) and unstimulated conditions. Shown are the raw unstimulated (A) and stimulated (B) images as well as the deconvolved unstimulated (C) and stimulated (D) images. The same cell from a monolayer is presented for direct comparison. The color bar denotes high and low  $[Ca^{2+}]$ .

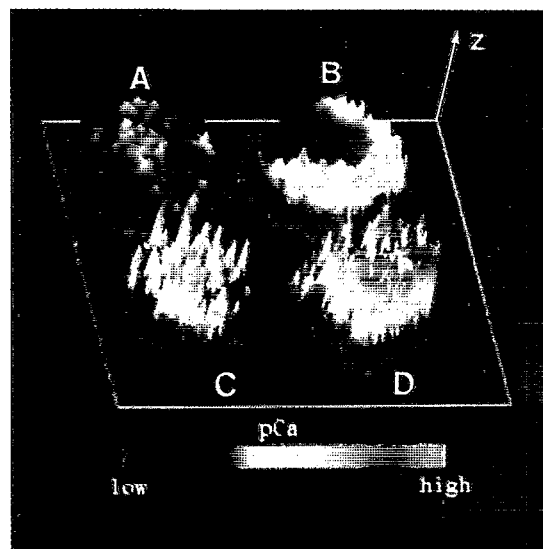


FIG. 17.  $[Ca^{2+}]$  distributions of the central optical slice of a BAEC under stimulated and unstimulated conditions. The images are the same as in Fig. 16, except that intensity (denoting concentration) has been plotted on the z-axis to facilitate easier viewing of concentration gradients and homogeneity.

The same cell is shown for direct comparison. A color bar is also provided to denote low and high calcium concentrations. Comparing the raw and deconvolved images under unstimulated conditions [Figs. 16(A) and 16(C)], there is a 15% increase in the whole cell ratio, a 59% decrease in the cell area, and a 52% decrease in the integrated intensity. Likewise, comparing the raw and deconvolved images under stimulated conditions [Figs. 16(B) and 16(D)], there is a 28% increase in the whole cell ratio value, a 52% decrease in the cell area, and a 34% decrease in the integrated intensity. The 15% and 28% increases in the unstimulated and stimulated whole cell ratio values, respectively, corresponds to a 23% and 43%

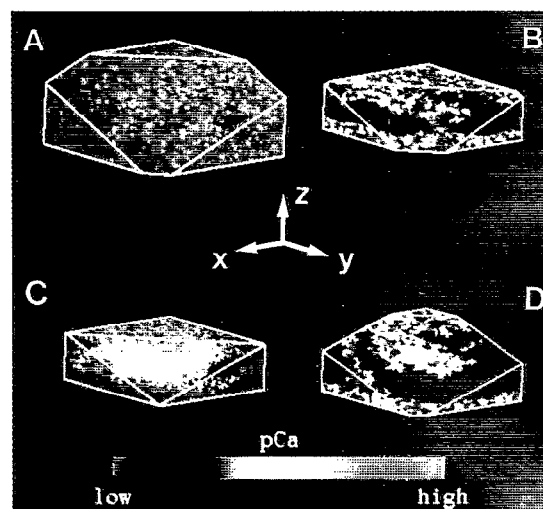


FIG. 18. Full 3D data sets of a BAEC under stimulated and unstimulated conditions. The 3D data has been digitally sliced at oblique angles to reveal a portion of the BAEC. The same portion of the BAEC is revealed on the exposed oblique plane.

increase in the average calcium concentration of the cell. Thus, the  $[Ca^{2+}]$  determined from raw, blurred images are greatly underestimated compared to the deconvolved images. Moreover, if one uses the raw images to determine the increase in  $[Ca^{2+}]$  due to ATP stimulation one obtains a 19% increase whereas if one uses the deconvolved images a 40% increase in  $[Ca^{2+}]$  is obtained. In contrast, Yelamarty *et al.* did not observe any significant difference in  $[Ca^{2+}]$  derived from raw ratio images and deconvolved ratio images of human erythroblasts.<sup>28</sup> However, they point out that small regions of higher  $[Ca^{2+}]$  may have been masked by contaminating light from adjacent planes since their nearest-neighbor deconvolution algorithm only takes into account three planes per optical slice. Our method uses the entire 3D data set during deconvolution. In a related study, Yelamarty & Cheung did observe a 17% increase in  $[Ca^{2+}]$  when comparing raw and deconvolved images of rat hepatocytes.<sup>27</sup> Waybill *et al.* similarly have shown that deconvolution of rat hepatocytes results in a 16% increase in whole cell  $Ca^{2+}$ , an 18% increase in the cytosolic  $Ca^{2+}$ , and no significant difference in nuclear  $[Ca^{2+}]$  estimates.<sup>64</sup>

Figure 17 shows the same image slices as depicted in Fig. 16 with intensity being plotted on the  $z$  axis. Plotting intensity on the  $z$  axis allows for easier viewing of concentration gradients and spatial homogeneity. There are several other points to note from Figs. 16 and 17. First, deconvolution of the raw images [Figs. 16(A), 16(B), 17(A), and 17(D)] increases the clarity and sharpness of the ratio images [Figs. 16(C), 16(D), 17(C), and 17(D)] and removes out-of-focus contamination, as evidenced by the decreased cell area and integrated intensity. Moreover, the calcium levels depicted in the raw, unstimulated images [Figs. 16(A) and 17(A)] show spatial homogeneity. On the other hand, the calcium levels in the corresponding deconvolved images [Figs. 16(C) and 17(C)] show spatial heterogeneity. There are local regions of high  $[Ca^{2+}]$  throughout the deconvolved images. This is in keeping with the notion that there are subcellular regions or organelles (like the endoplasmic reticulum) that have higher  $[Ca^{2+}]$  than the cytoplasm. In addition, when comparing the raw and deconvolved stimulated images [Figs. 16(B), 16(D), 17(B), and 17(D)] one observes that the  $[Ca^{2+}]$  gradient across the cell is preserved ( $[Ca^{2+}]$  increases as you travel from the top, left of the cell to the bottom, right). However, the region of higher  $[Ca^{2+}]$  covers a greater extent of the cell in the deconvolved images [Figs. 16(D) and 17(D)].

Figure 18 shows the full 3D data sets of the unstimulated raw and deconvolved data [Figs. 18(A) and 18(C)] as well as the stimulated raw and deconvolved data [Figs. 18(B) and 18(D)]. The 3D data were formed and volume rendered as discussed in Sec. III. The data were then digitally sliced at oblique angles to reveal a plane within the cells. Although each of the images has been cut at different angles, the displayed oblique planes reveal the same portion of the cell in each of the images. It can be appreciated that the deconvolved data sets are visually sharper and localized regions of high and low  $[Ca^{2+}]$  can be detected. The full 3D data sets can be digitally sliced at any angle and vectors can be spawned through the data sets and the  $[Ca^{2+}]$  plotted in vec-

tor space. In addition, the data sets can be rotated and animated movies can be recorded to display the calcium distributions as one digitally rotates the cells.

## VI. FURTHER CONSIDERATIONS

We have successfully developed a first generation technique that allows the quantification and visualization of intracellular ions in three dimensions. Whole cell fluorescent images are extremely difficult images to deconvolve, due to the amount of out-of-focus information present in these images. The technique makes use of available imaging technology and couples it with digital deconvolution to acquire and remove out-of-focus information using an experimentally determined PSF. The 1D, 2D, and 3D results in this study show that the deconvolution algorithm used for the image restoration works well in removing the out-of-focus information from fluorescent images. Furthermore, we have shown that substantial errors in  $[Ca^{2+}]$  measurement can occur if the 3D data are not first deconvolved. What is presently lacking, however, is the ability to map the calcium spatial distributions to subcellular organelles (nucleus or endoplasmic reticulum) or the cellular architecture. The inability to map  $[Ca^{2+}]$  to reference structural shapes makes the comprehension of the volume rendered data somewhat difficult. Future methods employed to interpret the 3D ion images may include labeling the BAECs with multiple fluorescent dyes. That is, Fura-2 labeling would be used for  $[Ca^{2+}]$  quantification and a second dye would be used to label a cellular organelle or cytoskeletal element. Alternatively, an optical series of phase or bright field images may be acquired along with the Fura-2 images. Even so, the results presented demonstrate that the restoration method is applicable for measuring the intracellular ion concentrations within cells. In addition, the spatial changes in the ion concentrations are readily visible using volume rendering.

The current application of the technique presented was initially developed specifically for measuring intracellular ion concentrations using specific fluorescent dyes. However, the technique is well suited for use with other fluorescent probes for investigating other interests. In addition, the technique is applicable to other forms of light microscopy, such as phase and bright field. One is limited only by the ability to acquire an appropriate PSF for the specific form of light microscopy.

## ACKNOWLEDGMENTS

We wish to thank Dr. S.G. Eskin and Lydia Sturgis at the Texas Biotechnology Corporation for their gift of the BAECs and tissue culture training. In addition, we wish to thank the W. M. Keck Center For Computational Biology at Rice for funding, in part, the purchase of the digital image processing system. This research was further supported by a Robert A. Welch Foundation Grant No. C-938 and two National Institutes of Health Grants Nos. R37-HL18672, NS-23316.

<sup>1</sup> A. Bhagyalakshmi and J. A. Frangos, *Biochem. Biophys. Res. Commun.* **158**, 31 (1989).

<sup>2</sup> P. F. Davies, J. C. F. Dewey, S. R. Bussolari, E. J. Gordon, and J. M. A. Gimbrone, *J. Clin. Invest.* **73**, 1121 (1984).

- <sup>3</sup>S. L. Diamond, S. G. Eskin, and L. V. McIntire, *Science* **243**, 1483 (1989).
- <sup>4</sup>S. L. Diamond, J. B. Sharefkin, C. Dieffenbach, K. Frasier-Scott, L. V. McIntire, and S. G. Eskin, *J. Cell Physiol.* **143**, 364 (1990).
- <sup>5</sup>S. G. Eskin, C. L. Ives, L. V. McIntire, and L. T. Navarro, *Microvasc. Res.* **28**, 87 (1984).
- <sup>6</sup>J. A. Frangos, L. V. McIntire, and S. G. Eskin, *Biotechnol. Bioeng.* **32**, 1053 (1988).
- <sup>7</sup>R. P. Franke, M. Grafe, H. Schnittler, D. Seiffge, and C. Mittermayer, *Nature* **307**, 648 (1984).
- <sup>8</sup>E. F. Grabowski, E. A. Jaffe, and B. B. Weksler, *J. Lab. Clin. Med.* **105**, 36 (1985).
- <sup>9</sup>M. J. Levesque, E. A. Sprague, C. J. Schwartz, and R. M. Nerem, *Biotechnol. Prog.* **5**, 1 (1989).
- <sup>10</sup>M. U. Nollert, E. R. Hall, S. G. Eskin, and L. V. McIntire, *Biochim. Biophys. Acta* **1005**, 72 (1989).
- <sup>11</sup>M. U. Nollert, S. G. Eskin, and L. V. McIntire, *Biochem. Biophys. Res. Commun.* **170**, 281 (1990).
- <sup>12</sup>M. U. Nollert, S. L. Diamond, and L. V. McIntire, *Biotechnol. Bioeng.* **38**, 588 (1991).
- <sup>13</sup>M. U. Nollert and L. V. McIntire, *J. Biomech. Eng.* **114**, 321 (1992).
- <sup>14</sup>S. P. Olesen, D. E. Clapham, and P. F. Davies, *Nature* **331**, 168 (1988).
- <sup>15</sup>S. R. Rajagopalan, L. V. McIntire, E. R. Hall, and K. K. Wu, *Biochim. Biophys. Acta* **958**, 108 (1988).
- <sup>16</sup>R. C. Ziegelstein, L. Cheng, and M. C. Capogrossi, *Science* **258**, 656 (1992).
- <sup>17</sup>J. Frangos, *Physical Forces and the Mammalian Cell* (Academic, San Diego, CA, 1993).
- <sup>18</sup>H. Hsieh, N. Li, and J. A. Frangos, *J. Cell Physiol.* **154**, 143 (1993).
- <sup>19</sup>M. J. Kuchan and J. A. Frangos, *Am. J. Physiol.* **264**, H150 (1993).
- <sup>20</sup>D. M. Spencer, T. J. Wandless, S. L. Schreiber, and G. R. Crabtree, *Science* **262**, 1019 (1993).
- <sup>21</sup>W. A. Carrington, K. E. Fogarty, L. Lifshitz, and F. S. Fay, in *Handbook of Biological Confocal Microscopy*, edited by J. B. Pawley (Plenum, New York, 1990), p. 151.
- <sup>22</sup>D. A. Agard, Y. Hiraoka, P. Shaw, and J. W. Sedat, in *Fluorescence Microscopy of Living Cells in Culture: Part B, Quantitative Fluorescence Microscopy-Imaging and Spectroscopy*, edited by Y. L. Wang, and D. L. Taylor (Academic, New York, 1989), p. 353.
- <sup>23</sup>D. A. Agard, Y. Hiraoka, and J. W. Sedat, *Proc. SPIE* **1161**, 24 (1989).
- <sup>24</sup>K. R. Castleman, *Digital Image Processing* (Prentice-Hall, Englewood Cliffs, NJ, 1979).
- <sup>25</sup>D. A. Agard, *Annu. Rev. Biophys. Bioeng.* **13**, 191 (1984).
- <sup>26</sup>P. J. Shaw, in *Electronic Light Microscopy: The Principles and Practice of Video-Enhanced Contrast, Digital Intensified Fluorescence, and Confocal Scanning Light Microscopy*, edited by D. Shotton (Wiley-Liss, New York, 1993), p. 211.
- <sup>27</sup>R. V. Yelamarty and J. Y. Cheung, *Proc. SPIE* **1660**, 606 (1992).
- <sup>28</sup>R. V. Yelamarty, B. A. Miller, J. R. C. Scaduto, F. T. S. Yu, D. L. Tillotson, and J. Y. Cheung, *J. Clin. Invest.* **85**, 1799 (1990).
- <sup>29</sup>J. R. Monck, A. F. Oberhauser, T. J. Keating, and J. M. Fernandez, *J. Cell Biol.* **116**, 745 (1992).
- <sup>30</sup>D. A. Agard and J. W. Sedat, *Proc. SPIE* **264**, 110 (1980).
- <sup>31</sup>Y. Hiraoka, M. C. Rykowski, J. A. Lefstin, D. A. Agard, and J. W. Sedat, *Proc. SPIE* **1205**, 11 (1990).
- <sup>32</sup>P. A. Jansson, *Deconvolution: With Applications in Spectroscopy* (Academic, New York, 1984).
- <sup>33</sup>M. Koshy, D. A. Agard, and J. W. Sedat, *Proc. SPIE* **1205**, 64 (1990).
- <sup>34</sup>C. Preza, M. I. Miller, J. L. J. Thomas, and J. G. McNally, *J. Opt. Soc. Am. A* **9**, 219 (1992).
- <sup>35</sup>W. Carrington and K. Fogarty, *Proceedings of the 13th Annual Northeast Bioengineering Conference 1987*, edited by K. Foster (IEBE), p. 108.
- <sup>36</sup>F. S. Fay, W. Carrington, and K. E. Fogarty, *J. Microsc.* **153**, 133 (1989).
- <sup>37</sup>F. S. Fay, W. Carrington, L. M. Lifshitz, and K. Fogarty, *Proc. SPIE* **1161**, 12 (1989).
- <sup>38</sup>W. A. Carrington, *Proc. SPIE* **1205**, 72 (1990).
- <sup>39</sup>Y. Hiraoka, J. W. Sedat, and D. A. Agard, *Biophys. J.* **57**, 325 (1990).
- <sup>40</sup>S. Inoue, *Video Microscopy* (Plenum, New York, 1986).
- <sup>41</sup>S. Inoue, in Ref. 22, p. 85.
- <sup>42</sup>H. Blumenfeld, L. Zablow, and B. Sabatini, *Biophys. J.* **63**, 1146 (1992).
- <sup>43</sup>B. R. Frieden, *J. Opt. Soc. Am.* **57**, 56 (1967).
- <sup>44</sup>N. Streibl, *J. Opt. Soc. Am.* **2**, 121 (1985).
- <sup>45</sup>A. Erhardt, G. Zinser, D. Komitowski, and J. Bille, *Appl. Opt.* **24**, 194 (1985).
- <sup>46</sup>I. T. Young, in Ref. 22, p. 1.
- <sup>47</sup>G. R. Bright, G. W. Fisher, J. Rogowska, and D. L. Taylor, in Ref. 22, p. 157.
- <sup>48</sup>B. Willis, B. Roysam, J. N. Turner, and T. J. Holmes, *J. Microsc.* **169**, 347 (1993).
- <sup>49</sup>S. R. Bolsover, R. A. Silver, and M. Whitaker, in Ref. 26, p. 181.
- <sup>50</sup>H. Schlichting, *Boundary Layer Theory* (McGraw-Hill, New York, 1979).
- <sup>51</sup>R. Tran-Son-Tay, in *Physical Forces and the Mammalian Cell*, edited by J. A. Frangos (Academic, New York, 1993), p. 1.
- <sup>52</sup>C. Preza, J. M. Ollinger, J. G. McNally, and J. L. J. Thomas, *Proc. SPIE* **1660**, 158 (1992).
- <sup>53</sup>S. G. Eskin, H. D. Sybers, L. Trevino, J. T. Lie, and J. E. Chimoskey, *In Vitro* **14**, 903 (1978).
- <sup>54</sup>R. Haugland, in *Fluorescent and Luminescent Probes for Biological Activity: A Practical Guide to Technology for Quantitative Real-Time Analysis*, edited by W. T. Mason (Academic, London, 1993), p. 34.
- <sup>55</sup>G. Grynkiewicz, M. Poenie, and R. Y. Tsien, *J. Biol. Chem.* **260**, 3440 (1985).
- <sup>56</sup>W. T. Mason, J. Hoyland, I. Davison, M. A. Carew, B. S. Sundaram, R. Tregear, R. Zoree, P. M. Liedo, G. Shankar, and M. Horton, in Ref. 54, p. 179.
- <sup>57</sup>D. A. Williams and F. S. Fay, *Cell Calcium* **11**, 75 (1990).
- <sup>58</sup>G. R. Bright, in *Optical Microscopy: Emerging Methods and Applications*, edited by B. Herman and J. J. Lemasters (Academic, San Diego, CA, 1993), p. 87.
- <sup>59</sup>A. Kaufman, *Volume Visualization* (IEEE Computer Society Press, Los Alamitos, CA, 1991).
- <sup>60</sup>J. P. Butler, J. A. Reeds, and S. V. Dawson, *SIAM J. Numer. Anal.* **18**, 381 (1981).
- <sup>61</sup>W. Carrington, Department of Mathematics, Ph.D. thesis, Washington University, 1982.
- <sup>62</sup>M. Mo, S. G. Eskin, and W. P. Schilling, *Am. J. Physiol.* **260**, H1698 (1991).
- <sup>63</sup>M. Lynch, J. I. Gillespie, and C. Johnson, *Cell Calcium* **13**, 227 (1992).
- <sup>64</sup>M. M. Waybill, R. V. Yelamarty, Y. Zhang, R. C. Scaduto, Jr., K. F. LaNoue, C. Hsu, B. C. Smith, D. L. Tillotson, F. T. S. Yu, and J. Y. Cheung, *Am. J. Physiol.* **261**, E49 (1991).